A&A 675, A205 (2023)
https://doi.org/10.1051/0004-6361/202245723

Astronomy & Astrophysics

Preparation for an unsupervised massive analysis of SPHERE high-contrast data with PACO

Optimization and benchmarking on 24 solar-type stars*

A. Chomez[1,2], A.-M. Lagrange[1,2], P. Delorme[2], M. Langlois[3], G. Chauvin[4], O. Flasseur[3], J. Dallant[3], F. Philipot[1], S. Bergeon[2], D. Albert[6], N. Meunier[2], and P. Rubini[5]

[1] LESIA, Observatoire de Paris, Université PSL, CNRS, 5 place Jules Janssen, 92190 Meudon, France
e-mail: `antoine.chomez@obspm.fr`
[2] Université Grenoble Alpes, CNRS, IPAG, 414 rue de la Piscine, 38000 Grenoble, France
[3] CRAL, UMR 5574, CNRS, Université de Lyon, ENS, 9 avenue Charles André, 69561 Saint Genis Laval Cedex, France
[4] Université Côte d'Azur, OCA, CNRS, Lagrange, CS 34229, 06304 Nice Cedex 4, France
[5] Pixyl S.A. La Tronche, 5 Av. du Grand Sablon, 38700 La Tronche, France
[6] Université Grenoble Alpes, CNRS, Observatoire des Sciences de l'Univers de Grenoble (OSUG), Grenoble, 122 rue de la Piscine, 38400 Saint-Martin-d'Hères, France

Received 19 December 2022 / Accepted 9 May 2023

ABSTRACT

Context. Despite tremendous progress in the detection and characterization of extrasolar planetary systems in the last 25 yr, we have not pinpointed any Solar System analogues. In particular, Jupiter-like planets (either mature or old) are barely detectable beyond 5 au with indirect techniques and they are still out of the reach of direct imaging techniques.

Aims. Our study is aimed at a search for exoplanets throughout the whole ESO/VLT-SPHERE archive with an improved and unsupervised data analysis algorithm that could allow us to detect massive giant planets at 5 au. To prepare, test, and optimize our approach, we gathered a sample of 24 solar-type stars observed with SPHERE using angular and spectral differential imaging modes.

Methods. We used PACO, a recently developed new-generation algorithm that has been shown to outperform classical methods. We also improved the SPHERE pre-reduction pipeline and optimized the outputs of PACO to enhance the detection performance. We developed custom-built spectral prior libraries to optimize the detection capability of the ASDI mode for both IRDIS and IFS.

Results. Compared to previous works conducted with more classical algorithms, the contrast limits we derived with PACO are more reliable and significantly improved, especially at short angular separations, where a gain by a factor ten has been obtained between 0.2 and 0.5 arcsec. Under good observing conditions, planets down to 5 M_{Jup}, orbiting at 5 au could be detected around stars within 60 parsec. We identified two exoplanet candidates that will require a follow-up to test for a common proper motion.

Conclusions. In this work, we use a small sample to demonstrate the benefits of PACO in terms of achievable contrast and of control of the confidence levels. In addition, we have developed custom tools to take full advantage of this algorithm and to quantity the total error budget on the estimated astrometry and photometry. This work paves the way towards an end-to-end, homogeneous, and unsupervised massive re-reduction of archival direct imaging surveys in the quest for new exo-Jupiters.

Key words. techniques: high angular resolution – techniques: image processing – methods: data analysis – instrumentation: adaptive optics – planets and satellites: detection

1. Introduction

Since the discovery of the first giant planets around solar-type stars almost 30 yr ago, thousands of planets have since been discovered, with masses down to a few Earth masses. However, Solar System analogues[1] have not been detected thus far, and so, we still do not know if our own planetary system is indeed unique. Detections of Earth twins have still not been made possible, as this requires major on-going research to correct for stellar activity with radial velocity (RV) techniques at the appropriate level (Meunier & Lagrange 2019). Also, detecting Jupiter twins orbiting at 5 au is very challenging (and not possible at larger separations) with radial velocity because decade(s) of careful monitoring are needed; additionally, long-term stellar activity is also responsible for a long-term noise. As a consequence, the orbital parameters of the (still rare) RV planets announced beyond 5 au are poorly characterized (Wittenmyer et al. 2016; Fernandes et al. 2019; Fulton et al. 2021). These limitations stand in the way of making precise comparisons between the radial distribution of giant planets beyond their forming regions and predictions from population synthesis models meant to constrain formation scenarios (Lagrange et al. 2023).

Giant planets (GPs) have played a significant role in the building of the Solar System (see e.g., Levison & Agnor 2003; Raymond et al. 2014; Morbidelli et al. 2012) and of exoplanetary systems (see e.g., Quintana & Barclay 2016; Childs et al. 2019). Various mechanisms may be involved, among which dynamical interactions with lighter bodies (e.g., telluric planets, planetesimals) once the proto-planetary disk has dissipated and the dynamics is no longer controlled by gas. In

---

* Detection table is only available at the CDS via anonymous ftp to `cdsarc.cds.unistra.fr` (`130.79.128.5`) or via `https://cdsarc.cds.unistra.fr/viz-bin/cat/J/A+A/675/A205`

[1] Defined as planetary systems around solar-type stars, hosting inner Earth-mass planets with at least one in the habitable zone, and outer sub-Jupiter/Jupiter masses planets.

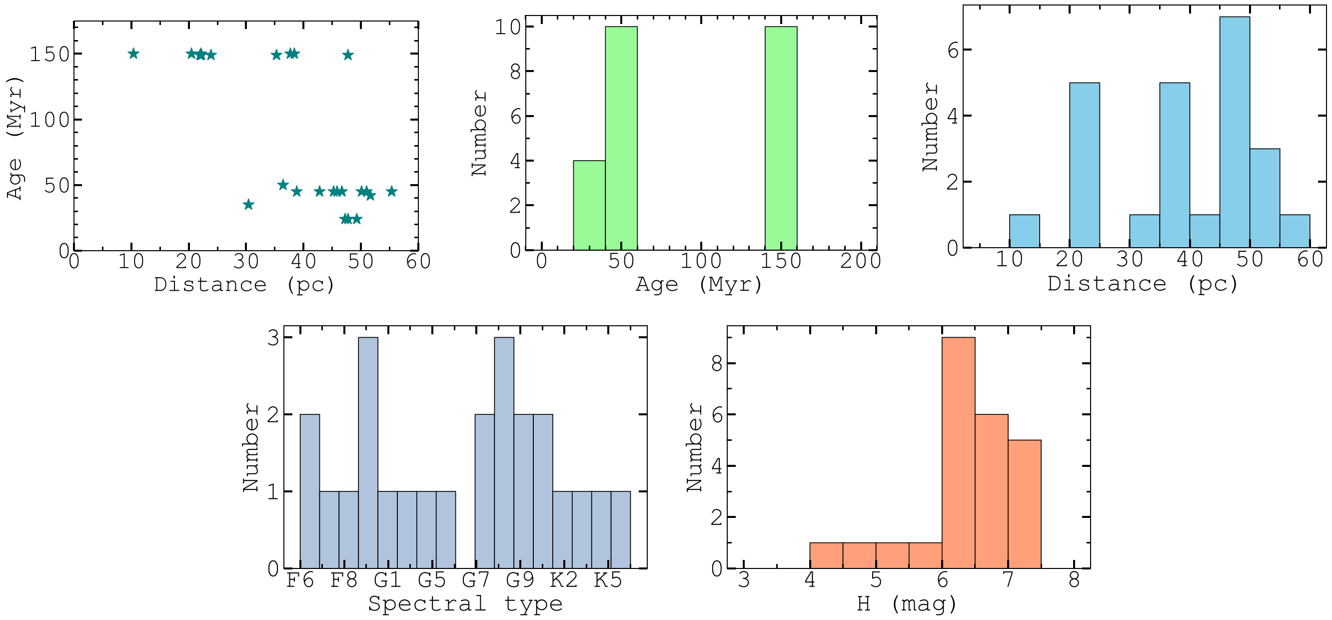

Fig. 1. Properties of the sample stars in terms of distance, age, spectral type, and magnitude.

particular, GPs may play a role in the development of life on Earth analogues (Horner & Jones 2010) and could even have driven the delivery of water on Earth (Morbidelli et al. 2012). From an observational point of view, remote GPs may also impact the detectability of lighter and closer-in planets with the RV technique and with astrometry because of the more complex RV or astrometric signals in case of multiple systems. Hence, knowing their giant planet population is key to modeling individual systems.

Detecting giant planets is therefore crucial to understanding planetary system formation and evolution. While RV or transit techniques are best suited to detect GPs orbiting typically within 5 au, they are not well adapted for detecting and characterizing more remote ones. Absolute astrometry is well adapted for giants in the 5–10 au (Perryman et al. 2014), even though such long period planets may be difficult to fully characterize (Ranalli et al. 2018), especially in the case of multiple systems. Microlensing will also be very useful to constrain the giant planet demographics in the 5–10 au range (Beaulieu & Bachelet 2021). High-contrast direct imaging (DI) is probably the most promising technique for detecting and characterizing analogues of our Solar System's giants planets in the future. Yet current high-contrast instruments like SPHERE (Beuzit et al. 2019) or GPI (Macintosh et al. 2014) are sensitive to massive young giants orbiting typically beyond 10 au. As an example, the SPHERE SHINE GTO survey had a 20% chance of detecting a 2 $M_{\rm Jup}$ at 20 au, and a 10% chance of detecting a 4 $M_{\rm Jup}$ planet at 5 au (Vigan et al. 2021). These poorer performances are due to 1) limitations at the instrumental and data processing levels and 2) a geometrical effect, namely: unless they are on pole-on orbits, short-period planets may be missed in a single observation because of a small projected separation at the time of the observation. For instance, due to geometrical effects, a single observation only allows us to explore half of the 5 au region around a star located 30 pc away when the planet orbit is seen edge-on. Fortunately, this geometrical effect can be easily overcome: the region explored is increased by more than 70% by observing the star twice, each time a few years apart (Lannier et al. 2017).

In this paper, we apply PACO (patch covariance), a promising detection algorithm (Flasseur et al. 2018, 2020a,b) on a small sample of stars representative of SPHERE targets, which are members of young close associations observed as part of the SPHERE/SHINE survey (Desidera et al. 2021) and observed under a wide range of atmospheric conditions. This analysis constitutes a test-bed for a forthcoming massive reduction of the SPHERE archive. Our aim is to find the best analysis strategy and to estimate the detection limits achievable on these stars. Moreover, we define our sample so as to address the astrophysical question of how far we are from detecting young giant planet siblings of our Solar System.

Our paper is organized as follows: the sample and the data are described in Sect. 2. The data reduction and analysis are described in Sects. 3 and 4, respectively. Section 5 describes the achievable performance and Sect. 6 presents the astrophysical results. A brief summary and a presentation of future work are provided in Sect. 7.

2. Star sample

Our sample is a collection of all (24) young (≤150 Myr), close by (<60 pc), solar-type stars (FGK) observed during the SPHERE/SHINE survey early science release (Desidera et al. 2021) and previously analyzed with conventional post-processing algorithms by (Langlois et al. 2021, hereafter, F150). The thresholds in age and distance were chosen to ensure the best detection limits (5 $M_{\rm Jup}$, down to possibly 1 $M_{\rm Jup}$) possibly down to 5–10 au from the stars, namely, at the locations of the Solar System giants[2]. Figure 1 and Table A.1 show the properties of the stars in our sample directly extracted from Desidera et al. (2021). It can be noted that the histogram of the ages of the considered stars is bimodal, with one subset aged between 20 and 60 Myr and the other aged about 150 Myr. This bimodal distribution is caused by some stars belonging to young co-moving groups such as AB Doradus (ABDO, 150 Myr), Tucana-Horologium (TUC, 45 Myr), Carina (CAR, 45 Myr), or β Pictoris (BPIC, 24 Myr).

---

[2] Our sample is therefore biased, and the present study is not meant to have a statistical value.

All our targets were observed in angular (and spectral) differential imaging (A(S)DI, Marois et al. 2006) using the telescope in pupil tracking mode. The standard observing mode of the SHINE survey, namely, the IRDIFS mode was used, with IRDIS dual band images in H2 and H3 (Dohlen et al. 2008) and IFS (Claudi et al. 2008) data covering the YJ bands[3]. Tables A.2 and A.3 provide descriptions of the observations and of the associated atmospheric conditions during these observations. The stars were observed around the time of the meridian crossing, to ensure the largest amplitude of parallactic angle variations (of at least 30 degrees). The atmospheric conditions were heterogeneous, with a seeing ranging from 0.5″ to 1.0″ most of the time and the coherence time ranging between 1 and 10 ms.

3. Data reduction and frame centering

The reduction pipeline from raw to centered datasets is similar to the one built for the SHINE survey, described in Delorme et al. (2017) and Langlois et al. (2021). To improve the centering of the IRDIS and IFS frames, a custom built routine that uses the waffle center calibration has been developed (Dallant et al. 2023). As part of the observing sequence, before and after the coronagraphic sequence, two coronagraphic images are recorded with a waffle pattern applied to the deformable mirror to create four replicas of the point spread function (PSF) at a separation of about 14 λ/D from the central star. These replicas, called "satellite spots", are used to determine precisely the position of the central star behind the coronagraphic mask before and after the long coronagraphic sequence.

To determine the accurate positions of the satellite spots, small circular regions are extracted around their theoretical positions and a bi-dimensional, non-istropic Gaussian fit is performed using a trust region reflective algorithm (Branch et al. 1999), particularly suited for large sparse problems with bound constraints. Estimates of the central star positions are then computed via the centroid of the resulting fitted satellite spots and their associated uncertainties. The frames are re-centered using the mean value of the two estimated centroids. This new routine is marginally more precise than the one currently implemented in the SPHERE data center, but its main advantage is a much faster computational time: assembling the 4D datacube takes only a few minutes, that is: more than one order of magnitude faster than the current pipeline, without any loss in precision.

We note that when precise astrometric measurements of known companions are needed, the satellite spots are generated during the whole coronagraphic sequence. In such cases, all frames are recentered individually using their own satellite spots.

4. Analysis pipeline

The analysis pipeline is based on the PACO A(S)DI pipeline described in Flasseur et al. (2020a,b). A few important upgrades were made, as follows: (1) an improvement in the PACO robustness, namely, the capability to run PACO on diverse and heterogeneous datasets, while consistently providing reliable results (see Sect. 4.1); (2) an optimization of spectral priors for PACO ASDI (see Sect. 4.2); (3) an automated and improved computation of astrometric and photometric error bars for each characterized source (see Sect. 4.3); and (4) an automated classification of the status of any identified candidate companion in case of multi epoch observations (see Sect. 4.4).

Finally, in view of the forthcoming massive re-reduction of all SPHERE data, a tool was developed to automatically identify any potential companion, and gather associated astrophysical information (astrometry, photometry, spectra, etc.) required for further analysis. These upgrades are described in the following subsections. Both the centering routines and the analysis pipeline are hosted on the COBREX data center, a modified and improved server based on the SPHERE data center.

4.1. Improvements of PACO robustness

The principle of the PACO algorithm is described in Flasseur et al. (2018). No fundamental modifications were made concerning the core and the technical elements of the methods. The main updates are: (1) a refinement of the PSF fitting routine, now implementing a robust strategy based on iteratively re-weighted least-squares (Huber 2011). This routine improves the robustness of the fit in the case of very low signal-to-noise ratio (S/N) in the measured off-axis PSF (e.g., in absorption bands); and (2) the management of time-variable missing data, with a time-variable mask, to account for possible evolution (during the sequence of acquisition) of the field-of-view with exploitable data.

In addition, an engineering effort has been made to validate, via numerical experiments, the faithfulness of the astrophysical quantities produced by the algorithm, particularly those concerning the astrometry and photometry, as well as their associated error bars. Due to residual noise, the flux estimate in the absence of a source is not completely zero on average. The average level of this effect was estimated for both ADI and ASDI. Thus, flux estimates for which the detection confidence is less than 1σ in ASDI and 2.5σ in ADI were not considered or used in this analysis or in the massive reduction. Along the same line, code upgrades (accelerations, automations, and case-specific handlings) have been implemented to allow for massive reductions performed on a computer server.

4.2. PACO ASDI spectral priors to increase the sensitivity

The ASDI mode of PACO offers the possibility to combine multi-wavelength datasets into a detection map, using specific weights to maximize the detection efficiency. These weights, $\{w_\ell\}_{\ell=1:L} \in [0; 1]$, are referred to as the spectral priors They are represented by vectors with as many components as wavelengths: $L = 2$ for IRDIS data and $L = 39$ for IFS. Since all the photometric measurements within PACO are expressed with respect to the target star, the priors should also be expressed as the expected companion contrast relative to the host star (shape-wise). They are then normalized between 0 and 1 (dynamic-wise). When simultaneously using multiple priors, the PACO algorithm computes the S/N of the detected source for each prior. As an illustration, we show in Fig. 2 the S/N measured on point sources considering various priors for IRDIS data in the case of an injected fake planet. In Fig. 3, we show the same kind of plot for an IFS dataset and a real point-like source: HD 206893b (Milli et al. 2017). A more classical ASDI spectral combination approach, as the one implemented in the PCA and TLOCI versions of the SPHERE data center, is somewhat similar[4] to the

---

[3] Although no observations using the K12/YJH filters combination are studied in this paper, the methodological developments presented in Sects. 3, 4, and 5 are treated without any loss of generality.

[4] In practice, PACO ASDI also accounts for a confidence weight estimated locally for each spectral channel, giving more weight to the spectral channels where the variance of the estimated flux is the lowest. This information is never accounted for in classical algorithms such as TLOCI and PCA.

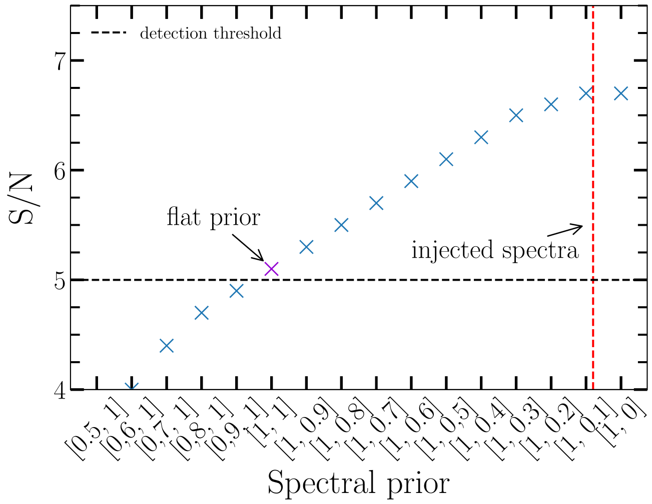

Fig. 2. Evolution of the S/N (blue) for various priors for a point source observed with IRDIS, and whose spectrum corresponds to the red mark. The x-axis gives various values of the priors. The S/N corresponding to the [0.5, 1] prior (significantly different from the normalized contrast of the injected source) is below the 4σ threshold used for this analysis, while the S/N reached for spectral prior [1, 0.1] (similar to the normalized contrast of the injected source) leads to a clear detection with a significance above the 5σ detection threshold (dashed black line).

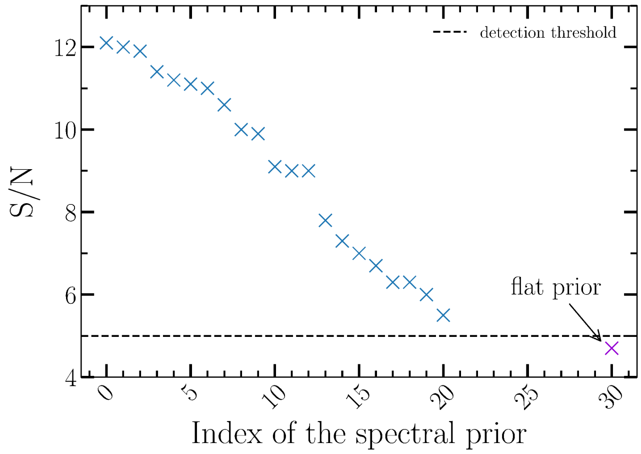

Fig. 3. Evolution of the S/N (blue) for various priors for HD 206893b (2017-07-13, IFS, YJ band). The x-axis gives the index of the priors. The S/N corresponding to the 10 last priors are below the 5σ detection threshold. Priors are ordered by decreasing S/N for clarity purposes. The S/N reached for spectral prior close to the spectrum (in contrast) leads to a detection with a significance above the 5σ detection threshold.

"flat prior" combination (i.e., assuming that the sought-for exoplanets have the same spectral energy distribution (SED) as their host stars), which is highlighted in Figs. 2 and 3.

As expected, the S/N is higher when the spectral prior is similar to the planet spectrum. Thus, we must define sets of spectral priors representative of the variety of the spectra of the potential exoplanets to optimize the detection capabilities. Besides, while increasing the number of priors improves the sensitivity to different types of objects[5], it also significantly increases the computational time and (moderately) increases the number of non-redundant false positives at a given detection threshold (see Sect. 4.2.2). A trade-off must then be found.

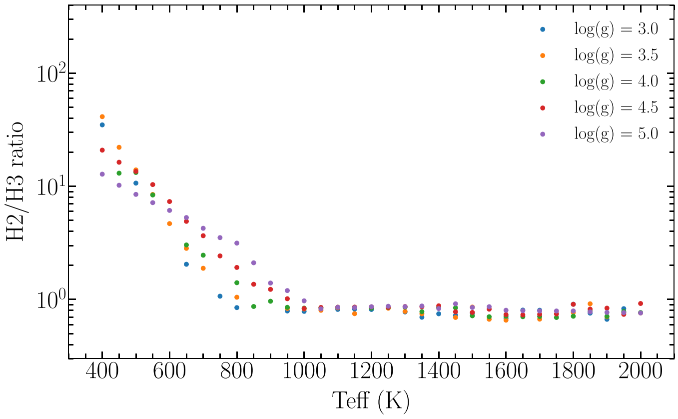

Fig. 4. Integrated H2/H3 flux ratio computed for a planet with a solar metallicity, C/O=0.50, and with different values of $\log(g)$ and T_{eff}. ExoREM spectra were used.

4.2.1. Selection of spectral priors using fake planets injections

To select the spectral priors, we used a set of four targeted stars that were used in a recent internal blindtest conducted by the SHINE consortium that was aimed at comparing the performance of various detection and characterization algorithms. The targets properties are provided in Table A.4, and the observing and atmospheric conditions are given in Table A.5. Several hundreds fake planets with various properties were randomly injected between 0.12″ and 5.5″ in the case of IRDIS data – while still avoiding any blending among injected sources. For IFS data, about 100 fake point sources (FPSs) were injected. The injected FPS spectra were taken from the BT-Settl grid (Allard 2014) and the priors were built using the ExoREM (Charnay et al. 2019) spectra. We purposely used different models to inject the fake planets and to build the priors, to avoid biases that could occur when using the same library for both the injection process and the prior definition.

4.2.2. Priors selection for IRDIS

To find the trade-off between sensitivity and computation time, we considered all possible available spectra, and for each raw spectrum, we computed the ratio $\frac{\mathrm{H2}}{\mathrm{H3}}$ (or $\frac{\mathrm{K1}}{\mathrm{K2}}$), where H2 and H3 (respectively K1 and K2) represent the integrated fluxes in these spectral bands. Figures 4 and 5 show examples of such ratios for a source with various effective temperatures, a solar metallicity and a C/O ratio of 0.5 for both filter combination. Two regimes can be identified: (i) a "cold" one, corresponding to T_{eff} roughly below 1000 K, where the $\frac{\mathrm{H2}}{\mathrm{H3}}$ (resp $\frac{\mathrm{K1}}{\mathrm{K2}}$) ratio varies from several tens even hundreds down to 1 mostly because of strong CH_4 absorption in H3 and K2 filters, and (ii) a "hot" one, corresponding to T_{eff} above 1000 K, where this ratio is almost constant between 1 and 0.6. A similar behavior is observed for all metallicities and C/O ratio.

The goal is to find the optimal number of priors to explore these features. To do so, we proceeded as follows:

We first used all the injected FPSs and measured in each case the S/N considering different priors. These priors correspond to

---

[5] It has been shown in Flasseur et al. (2020b) that the S/N of detection is only marginally degraded in the case where the prior SEDs differ significantly from the true SED of the sources. In any case, the probability of false alarms remains controlled at the prescribed detection threshold τ.

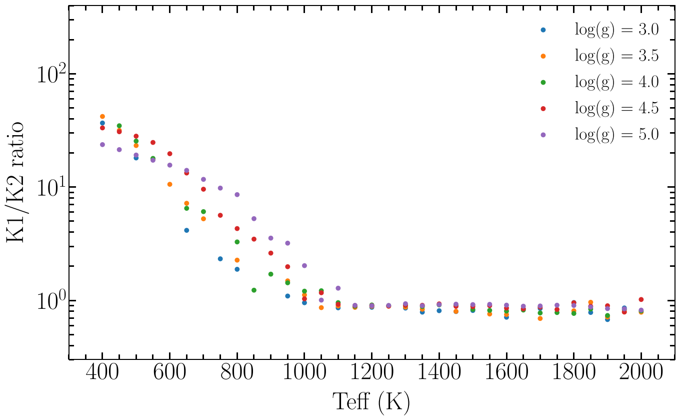

Fig. 5. Integrated K1/K2 flux ratio computed for a planet with a solar metallicity, C/O = 0.50, and with different values of $\log(g)$ and T_{eff}. ExoREM spectra were used.

the 15 priors showed in the x-axis of Fig. 2. In this example, the maximum S/N is 6.7. We then repeated the process using instead eight spectral priors uniformly spread over the considered parameter space (by steps of 0.2), five (by steps of 0.3), and four (by steps of 0.4). We then considered the evolution of the maximum S/N as a function of the number of priors (for each injected FPS). In the case of relatively faint FPSs (sources that cannot be identified on a single frame), using five priors (or more) does not significantly degrade the S/N (less than 1%), while using four (or less) does.

Second, we then studied the impact of the number of priors (between 1 and 8) on the rate of false positives. To do so, we computed the average number of false positives identified by PACO in the IRDIS FoV (limited to 5.5″ to avoid edge effects) on a total of 20 datasets and compared it to the theoretical value. We can compute the theoretical expected number of false positives as follows: because the pixel distribution on the S/N maps is Gaussian, the number N_{fp} of false positive per map according to the number n_{pixel} of pixels processed and the probability of false alarm $P_{\mathrm{FA}}(\tau)$ at a given detection threshold τ:

$$N_{\mathrm{fp}} = n_{\mathrm{pixel}} \times P_{\mathrm{FA}}(\tau)\,. \tag{1}$$

As an illustration, the number of pixels to process in each IRDIS dataset is approximately equal to one million and, with a 5σ detection confidence (i.e., $\tau = 5$, $P_{\mathrm{FA}}(5) \simeq 2.87 \times 10^{-7}$), we have:

$$N_{\mathrm{fp}} \simeq 10^6 \times 2.87 \times 10^{-7} \sim 0.287,$$

with false alarms expected in each detection map.

Figure 6 shows the results for $\tau = 5$ with an increasing number of spectral priors used. The false positive rate when considering a single S/N map corresponding to a given prior (no matter which prior is used) is in good agreement with what is expected from a Gaussian noise distribution (see Eq. (1)). When working with several priors, the number of detections will only increase if a new independent source (i.e., detected for the first time in the current prior) is detected. Redundant detections will only be accounted for one source. Because false positives are often redundant, the empirical cumulative false positive rate is lower than the theoretical cumulative one (i.e., if all false positives were independent).

This confirms the Gaussian nature of the S/N map produced by PACO as well as the associated statistical guarantees (i.e., control of the probability of false alarms and of detections). Based on this study, we chose to include five spectral priors in our library $\boldsymbol{\Omega}_{\mathrm{IRDIS}} \in \mathbb{R}^{2\times 5}$, achieving the desired trade-off between maximizing our detection performance and lowering the number of false positives:

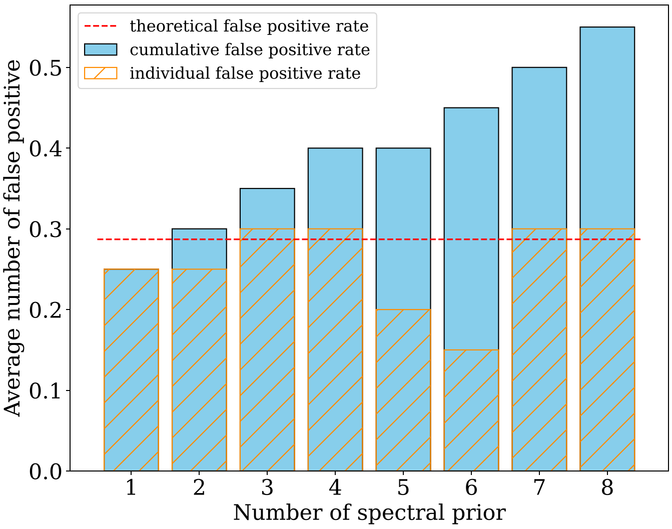

Fig. 6. Average number of false positives for a detection threshold $\tau = 5$ with one to eight spectral priors with IRDIS. Twenty observations were considered for these experiments. The red dashed line shows the theoretical false positive rate on a single S/N map. The mean experienced false positive rate for each S/N considered independently map is represented by the yellow dashed rectangles and the mean experienced cumulative false positive rate by the blue rectangles.

$$\boldsymbol{\Omega}_{\mathrm{IRDIS}} = \{[1, 1]; [1, 0.7]; [1, 0.4]; [1, 0.1]; [0.8, 1]\}\,.$$

4.2.3. Priors selection for IFS

In this section, we describe how we build a library $\boldsymbol{\Omega}_{\mathrm{IFS}} \in \mathbb{R}^{N\times L}$ of N spectral priors for processing the IFS data with PACO ASDI.

Following the notation introduced in Sect. 4.2, each element $\boldsymbol{w} \in \mathbb{R}^{L}$ of $\boldsymbol{\Omega}_{\mathrm{IFS}}$ is a vector with as many components as wavelengths (i.e., $L = 39$ for the IFS). In practice, we build a different set $\boldsymbol{\Omega}_{\mathrm{IFS}}$ for each stellar spectral type since each element $\boldsymbol{w}$ should be expressed in contrast units, so that it depends on the spectral type of the star explicitly. For the purposes of illustration, the method is described for any given stellar spectral type without loss of generality. The set $\boldsymbol{\Omega}_{\mathrm{IFS}}$ is built from a set $\boldsymbol{\Omega}_{\mathrm{ER}} \in \mathbb{R}^{N_{\mathrm{ER}}\times L_{\mathrm{ER}}}$ of sub-stellar spectra provided by the ExoREM models. The spectral resolution L_{ER} of each element $\boldsymbol{w}_{\mathrm{ER}} \in \mathbb{R}^{L_{\mathrm{ER}}}$ is much larger than L, with a typical value of $L_{\mathrm{ER}} = 500$ for this study.

For a given stellar spectrum, $\boldsymbol{s} \in \mathbb{R}^{L_{\mathrm{ER}}}$, and a sub-stellar spectrum, $\boldsymbol{w}_{\mathrm{ER}} \in \mathbb{R}^{L_{\mathrm{ER}}}$, at the same spectral resolution, L_{ER}, we obtained an (intermediate) spectral prior $\boldsymbol{w}' \in \mathbb{R}^{L_{\mathrm{ER}}}$ by dividing the two elements component-wise, namely: $w'_\ell = w_{\mathrm{ER}\,\ell}/s_\ell\,, \forall \ell \in [\![1; L_{\mathrm{ER}}]\!]$. Each intermediate spectral prior $\boldsymbol{w}'$ is then normalized by the maximum value over its components. The last operations aim to reshape $\boldsymbol{w}'$ from $L_{\mathrm{ER}} = 500$ to the spectral resolution, L, of the measurements by first applying a convolution with a Gaussian kernel of standard-deviation in the order of magnitude of L (typically between 30 and 50) and then re-sampling the results at the targeted spectral resolution L to get a final spectral prior $\boldsymbol{w}$.

Algorithm 1: Pseudo-code of the selection procedure of IFS spectral priors for PACO.

```
Input: ExoREM set $\boldsymbol{\Omega}_{\rm ER}$ of sub-stellar spectra.
Input: ExoREM spectrum $\boldsymbol{w}_{\rm ER}^{\rm ref}$ of reference.
Input: Stellar spectrum $\boldsymbol{s}$.
Input: Target number $N$ of spectral priors.
Input: Gaussian kernel $\boldsymbol{g}_L$ of width $L$.
Input: Sampling operator $\mathbf{R}_{L_{\rm ER}/L}$ by $L_{\rm ER}/L$.
Output: Library $\boldsymbol{\Omega}_{\rm IFS}$ of spectral priors.

▶ Step 1. Normalizing sub-stellar spectra.
$\boldsymbol{\Omega}' \leftarrow \{\}$ ;                                      (initialization)
for $j = 1$ to $N_{\rm ER}$ do
    $\boldsymbol{w}_{\rm ER} \leftarrow \boldsymbol{\Omega}_{{\rm ER}\,j}$ ;                        (get sub-stellar spectrum)
    $w'_\ell \leftarrow w_{{\rm ER}\,\ell}/s_\ell\,, \forall \ell \in [\![1; L_{\rm ER}]\!]$ ;             (normalization)
    $\boldsymbol{w}' \leftarrow \boldsymbol{w}' \circledast \boldsymbol{g}_L$ ;                         (Gaussian convolution)
    $\boldsymbol{w}' \leftarrow \mathbf{R}_{L_{\rm ER}/L}(\boldsymbol{w}')$ ;                       (re-sampling)
    $\boldsymbol{\Omega}' \leftarrow \{\boldsymbol{\Omega}' \cup \boldsymbol{w}'\}$ ;                        (storing)

▶ Step 2. Building library of spectral priors.
$\boldsymbol{w}^{\rm ref} \leftarrow \boldsymbol{\Omega}'_1$ ;                              (get reference spectral prior)
$\boldsymbol{\Omega} \leftarrow \{\boldsymbol{w}^{\rm ref}\}$ ;                                (initialization)
while card($\boldsymbol{\Omega}$) < $N$ do
    for $i = 1$ to card($\boldsymbol{\Omega}$) do
        $\boldsymbol{w} \leftarrow \boldsymbol{\Omega}_i$ ;                                (get a spectral prior)
        for $j = i$ to $N_{\rm ER}$ do
            $\boldsymbol{w}' \leftarrow \boldsymbol{\Omega}'_j$ ;                       (get a candidate spectral prior)
            $d_{i,j} \leftarrow \|\boldsymbol{w} - \boldsymbol{w}'\|_2^2$ ;                   (compute distance)
        $(\_, j^{\max}) \leftarrow \mathrm{argmax}_{i,j}(d_{i,j})$ ;              (get max index)
        $\boldsymbol{\Omega} \leftarrow \{\boldsymbol{\Omega} \cup \boldsymbol{\Omega}'_{j^{\max}}\}$ ;                      (storing)
$\boldsymbol{\Omega}_{\rm IFS} \leftarrow \boldsymbol{\Omega}$
```

We aimed to include in $\boldsymbol{\Omega}_{\rm IFS}$ the minimum number N of spectral priors needed to represent the diversity of the observations. For that purpose, we build $\boldsymbol{\Omega}_{\rm IFS}$ from a large set $\boldsymbol{\Omega}_{\rm ER}$ (i.e., $N_{\rm ER} \gg N$), and we progressively add non-redundant atoms $\boldsymbol{w}$ in $\boldsymbol{\Omega}_{\rm IFS}$. We first started with a single spectral prior $\boldsymbol{w}^{\rm ref}$ of reference in the set $\boldsymbol{\Omega}_{\rm IFS}$. This spectral prior is built from a sub-stellar model $\boldsymbol{w}_{\rm ER}^{\rm ref}$ of reference obtained from the ExoREM simulator with the following parameters: $T_{\rm eff}$ = 1000 K, Fe/H = 1.0, C/O = 0.50, and log(g) = 4.0. By looping over the (fixed) elements of $\boldsymbol{\Omega}_{\rm ER}$, we compute the Euclidean distance between each resulting candidate spectral prior and the spectral priors already present in $\boldsymbol{\Omega}_{\rm IFS}$. To the set $\boldsymbol{\Omega}_{\rm IFS}$, we then added the candidate spectral prior that maximized the distance, namely, the spectral prior that differs the most from the already selected ones. For practical reasons, we preset the number, N, of targeted elements in $\boldsymbol{\Omega}_{\rm IFS}$ to perform the above selection procedure. We repeated this procedure for various values of N and selected the number that gives a satisfying trade-off between precision and recall, while simultaneously leading to a manageable computation time at data reduction time. As an illustration, we find that reducing the number N of spectral priors in $\boldsymbol{\Omega}_{\rm IFS}$ from 31 to 20 decreases the detection capabilities only marginally (by less than 1% in terms of S/N loss). In addition, we find that decreasing the number N of spectral priors in the same proportion does not significantly impact the false positive rate (see Fig. 7). To more significantly decrease the false positive rate, it seems better to select $N \leq 13$. However, doing so would result in a significant decrease in the detection capabilities (by more than 15% in terms of S/N loss). As a conclusion of this study, we choose N = 20 spectral priors for the IFS instrument. This number is driven by a trade-off between precision and recall, namely, in order to keep the S/N loss sufficiently small, while limiting the number of false positives to a value similar to the IRDIS one.

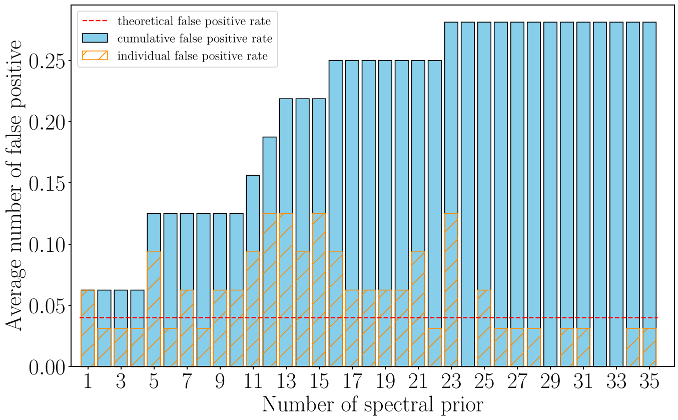

Fig. 7. Number of false positives experienced at detection time when using between N = 1 and N = 31 spectral priors with IFS. The detection threshold is set at τ = 5, and the results are averaged over 32 observations. The red dashed line shows the theoretical false positive rate on a single S/N map. The mean experienced false positive rate for each S/N considered independently map is represented by the yellow dashed rectangles and the mean experienced cumulative false positive rate by the blue rectangles.

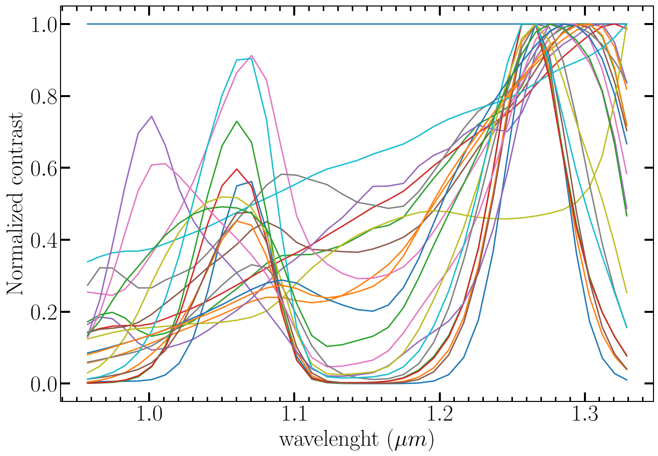

Fig. 8. Example of the library $\boldsymbol{\Omega}_{\rm IFS} \in \mathbb{R}^{20\times39}$ of spectral priors built for a G2 star in YJ bands. Priors are expressed in contrast unit and are normalized between 0 and 1. We systematically included in the library a "flat" spectral prior giving the same weights to all spectral channels.

The whole optimization process for a given stellar spectral type and for a targeted number N of spectral priors is described in the form of a pseudo-code by Algorithm 1. This selection procedure was repeated for all stellar spectral types considered in this work. Figure 8 shows an example of such built library of spectral priors for a G2 star observed in YJ bands.

Based on the built library of spectral priors, we can now, as for IRDIS, compare the empirical false positive rate with the theoretical value. We can again use Eq. (1) with the number of processed pixels for IFS $n_{\rm pixel}$ = 140 000. We find $N_{\rm fp}$ = 0.04 for IFS. We can see with Fig. 7 that (as for IRDIS) the false positive rate when considering individual S/N map is in good agreement with what is expected from a Gaussian noise distribution.

4.3. Refined astrometric and photometric error budgets

The PACO algorithm provides only fitting errors for both photometric and astrometric measurements. To get a complete error budget, we need to take into account other sources of errors.

For the astrometry error budget, we use both the results of the F150 analysis with the SpeCal pipeline (Langlois et al. 2021) and the calibration obtained by Maire et al. (2021). However, the F150 analysis used an average value of the typical centering error. Thanks to the improved frame centering routine described in Sect. 3, we are able to derive a precise estimate of this error on each data set and we propagate it through the whole pipeline .

For the photometry error budget, we used, for the first time, the differential tip-tilt sensor (DTTS, Baudoz et al. 2010, see Sect. 4.3.2 for the details) measurements to derive proper photometric error bars. Although such a precise analysis has already been done on specific targets for some particular studies, nothing was implemented routinely to perform massive analysis. This new analysis allows us to perform a complete, accurate, automated, and homogeneous error estimation for both astrometry and photometry.

4.3.1. Astrometric error budget

The PACO algorithm provides an astrometric fitting error term, hereafter denoted $\sigma_{\text{sep, PACO}}$ and $\sigma_{\text{PA, PACO}}$, associated, respectively, to the angular separation (sep) and to the parallactic angle (PA) of a given signal. Several additional sources of errors induced by pre-processing steps, such as the recentering of the individual frames, or systematics related to SPHERE itself must be considered. We therefore combine several additional terms to refine the global error budget. The uncertainties associated with the separation and PA are found as follows. For the uncertainties on the angular separation, we combined four terms:

A distortion error of 0.4 mas at 1 as (Maire et al. 2021), scaling linearly with the separation of a source:

$$\sigma_{\text{dist}}\,(\text{as}) = \text{sep (as)} \times \frac{0.4}{1000}. \tag{2}$$

A plate scale error, scaling linearly with the separation of a source. This plate scale and the associated error bars are measured during each observing run (astrometric calibration, see Langlois et al. (2021):

$$\sigma_{\text{platescale}}(\text{as}) = \frac{\text{sep (as)}}{\text{platescale}} \times \text{err}_{\text{platescale}}. \tag{3}$$

An error on the re-centering of the individual frames, as estimated by the re-centering procedure described in Sect. 3:

$$\sigma_{\text{recentering}}(\text{as}) = \sigma_{\text{recentering}}(\text{pxl}) \times \text{platescale}. \tag{4}$$

PACO internal error $\sigma_{\text{sep, PACO}}$.

Those 4 terms are quadratically combined to obtain the full error budget $\sigma_{\text{sep,tot}}(\text{as})$.

For the uncertainties on the PA, we also combine four terms: An error on the pupil angle equal to 0.52 mas at 1 as (Maire et al. 2021), scaling linearly with the separation:

$$\sigma_{\text{PA angle}}(^{\circ}) = \arctan\left(\frac{0.52}{1000} \times \text{sep (as)}\right) \times \frac{180}{\pi}. \tag{5}$$

An error associated with the true North, as measured using the astrometric calibrations, $\sigma_{\text{TN}}(^{\circ})$. An error on the re-centering of the individual frames, as estimated by the re-centering procedure (see Sect. 3):

$$\sigma_{\text{recentering}}(^{\circ}) = \frac{\sigma_{\text{recentering}}(\text{as})}{\text{sep (as)}} \times \frac{180}{\pi}. \tag{6}$$

PACO internal error $\sigma_{\text{PA, PACO}}(^{\circ})$.

Those four terms are also quadratically combined to obtain the full error budget $\sigma_{\text{PA,tot}}(^{\circ})$.

4.3.2. Photometric error budget

Our aim here is to estimate the relative photometric uncertainties using SPARTA data (Suárez Valles et al. 2012) as well as using information from the DTTS. The DTTS is a control organ of SPHERE that ensures the star is always well centered on the coronagraph. It diverts a small fraction of the stellar light to produce an image of the star, allowing us to have a direct access to a PSF during the observation. While this PSF is not exactly the same as it would be on the science cameras due to non-common aberrations, it can still be used to monitor the photometric variability during the observing sequence. In the following, these series are denoted by DTTS(t) as a function of the time t of observation. SPARTA is the real time control computer of the adaptive optics system. Over the course of an observation, SPARTA collects information on the observing conditions that are then stored. As for the astrometry, the PACO algorithm provides a fitting photometric error σ_{PACO}, but additional terms are needed to estimate the global error budget, as follows.

First, there is the error associated with the flux calibration of the coronagraphic frames using the PSF. Because the observing conditions vary during the observing sequence, this error is time-dependent. Using datasets with bright background companions, detectable with a high S/N on each individual frame, we found that the flux variations are well correlated with the Strehl ratio (SR) variations as provided by SPARTA[6]. Besides, the photometry of our faint sources cannot be estimated on each frame. Hence, we used the time series SR(t) data taken during the observation to estimate an average photometric error over the whole coronagraphic sequence.

Because SPARTA provides the SR at 1.6 μm, we compute the Strehl ratio $\text{SR}_{\lambda_{\text{i}}}(t)$ at the working wavelength of λ_{i} by using the following approximation – based solely on the adaptive optics fitting error and the Maréchal approximation (Maréchal 1948) – to capture the wavelength dependency for good conditions:

$$\text{SR}_{\lambda_{\text{i}}}(t) = \text{SR}(t)^{\left(\frac{1.6}{\lambda_i}\right)^2}. \tag{7}$$

Then, we computed the standard deviation of the SR, after removing the values for rejected frames, as follows:

$$\text{var}_{\text{flux},\lambda_i} = \frac{\sigma(\text{SR}_{\lambda_{\text{i}}}(t))}{\text{SR}_0}, \tag{8}$$

---

[6] https://www.eso.org/sci/facilities/develop/ao/tecno/sparta.html

where SR_0 is the SR of the PSF used. In PACO, it is the average between the off-axis PSF taken before the observing coronagraphic sequence and the one after. The error associated to the extracted spectra at each wavelength λ_i is therefore:

$$\sigma_{\mathrm{norm},\lambda_i} = \mathrm{spectra}_{\lambda_i} \times \mathrm{var}_{\mathrm{flux},\lambda_i}. \tag{9}$$

It sometimes happens that no SPARTA data are available. In such a case, the error is computed using the difference between the two available PSFs.

Second, there is the sky transparency: this term is measured thanks to the DTTS. While the peak of the DTTS PSF is also linked to the SR variation recorded by SPARTA, the total integrated flux from the DTTS PSF directly relates to the evolution of the sky transparency, but does not provide an absolute photometric measurement. By estimating the DTTS flux, we estimate the median and standard-deviation of the sky transparency variations over the coronagraphic sequence:

$$\mathrm{var}_{\mathrm{transp}} = \frac{\sigma(\mathrm{DTTS}(t))}{\mathrm{median}(\mathrm{DTTS}(t))}, \tag{10}$$

$$\sigma_{\mathrm{transp},\lambda_i} = \mathrm{spectrum}_{\lambda_i} \times \mathrm{var}_{\mathrm{transp}}. \tag{11}$$

Lastly, we have the PACO internal error σ_{PACO}. Those three terms are then quadratically summed to obtain the full photometric error budget.

4.4. Multi-epoch discrimination tool

Second epoch observations are crucial to test whether a signal is due to a source gravitationally bound to the target star. We developed a tool that automatically performs this analysis. In cases where the candidate is not recovered, it computes the false positive probability, given the detection limits achieved for the second epoch.

In practice, we first checked whether a source is detected in the second epoch data at the position expected from a background object, knowing the proper motion of the star[7]. This step allows us to identify the background sources (providing that the detection limits of the second epoch data set are good enough). If the signal cannot be associated with a background source, we search for a fainter signal (detected at $\tau \geq 4$) within a disk D centered on the position of the source at the first epoch, and with a radius corresponding to the motion of a gravitionally bound object orbiting on a circular pole-on orbit (corresponding to the maximum possible motion in projected separation). If a signal is found, we attribute it to a possible companion. In case of an ambiguous choice (i.e., the motion of the object can be associated either with a background source or a gravitionally bound source) a flag is raised to report the ambiguity. If no signal is found, we check whether the non-detection in the second epoch is due to poorer conditions or to the fact that the first detection was a false positive. To do so, we carried out the following steps.

First, we compute the S/N (labeled as S/N_2) that the signal should have in the second epoch using the second epoch contrast[8] map. Next, we measured the maximum S/N in the disk area in the second epoch data (S/N_{max}). Finally, as the S/N maps follow a centered Gaussian distribution with a unit variance, we can estimate the probability p of the source to be a real signal:

$$p = \int_{-\infty}^{S/N_{\mathrm{max}}-S/N_2} \frac{1}{\sqrt{2\pi}} e^{-0.5x^2}\,\mathrm{d}x. \tag{12}$$

5. Contrast comparison with other algorithms

Here, we present the contrast performance achieved by PACO on both IRDIS and IFS and compare them with the performance achieved by TLOCI (Marois et al. 2014) and PCA ADI (Soummer et al. 2012; Amara & Quanz 2012) for IRDIS, and TLOCI and PCA ASDI for IFS (Mesa et al. 2015). Those algorithms were used for the analysis of the SHINE F150 survey (Langlois et al. 2021). They are implemented in the SpeCal package (Galicher et al. 2018) dedicated to the analysis of the SHINE data with the following characteristics:

For TLOCI, the stellar profile is estimated frame by frame for each pixel in the field of view. The estimation uses a linear combination of all data to minimize the residuals after subtraction. The area on which the optimization is computed is much bigger than the subtraction area, thus mitigating as best as possible the self-subtraction of point-like sources. The Specal implementation of TLOCI also assumes a flat planet spectrum in contrast. The parameters for TLOCI were set as they were in the F150 reduction, as follows.

First, the optimization zone was separated by 0.5 full width at half maximum (FWHM) from the region of interest to avoid bias in the linear combination in case of the presence of a source in the region of interest. Next, the radial width (in radius) of the subtraction zone was set to one FWHM; Then, the radial to azimuthal ratio of the subtraction zone was set to 1.5; Finally, the optimization zone area was set to 20 PSF FWHM.

Both PCA algorithms are based on the equations described in Soummer et al. (2012). For IRDIS (ADI processing), the principal components (PCs) are computed independently for each spectral channel. For IFS (ASDI processing), the PCs are computed using the spatial and spectral dimensions simultaneously. For IRDIS, 5 PCs were used, and for IFS, 50, 100 and, 150 PCs were used.

The throughput of both TLOCI and PCA was estimated internally by SpeCal at each location in the field of view by generating a datacube with fake planets. The 1D throughput curve is then applied to the residual maps of both algorithms.

The contrast curves and maps were estimated for each spectral channel by computing the pixel by pixel azimuthal standard deviation in an annulus of 0.5 FWHM on the residual maps, once it had been corrected from the throughput. The 5σ detection limits are derived from this estimation by taking into account several corrections: the flux loss from ADI subtraction, the coronograph transmission, and the neutral density of the off-axis PSF. Finally, these detection limits were normalized by the off-axis PSF flux. The S/N maps were directly derived from the estimated flux and its associated standard-deviation (i.e., contrast at 1σ).

In Sect. 5.1, we present the contrast comparison between PACO and the algorithms described above. Since this direct comparison of contrast is biased by the diverse hypotheses made by each algorithm, we then present in Sect. 5.2 a set of numerical experiments resorting to massive injections of FPSs. This demonstrates the reliability of the contrast curves obtained with PACO, as well as the gain in sensitivity and control of the probability of false alarms compared with the two other algorithms.

5.1. Contrast performance

Figure 9 shows the predicted 5σ contrast as a function of the angular separation on IRDIS (with Fig. 10 showing the same but for IFS) obtained with the three considered algorithms for all epochs of the 24 stars considered in this study. For this

---

[7] Provided by Simbad: `http://simbad.u-strasbg.fr/simbad/`

[8] The contrast is estimated by averaging the contrast in the disk D.

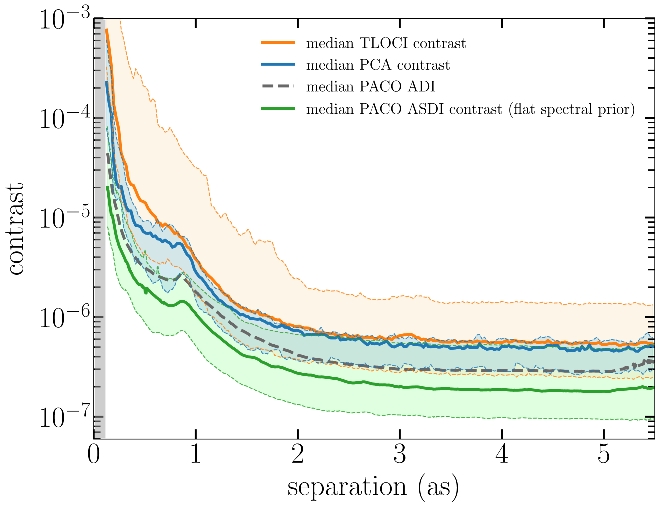

Fig. 9. Contrast comparison at 5σ between PACO, TLOCI, and PCA for IRDIS for the 24 science stars considered in this paper. A flat prior was used for PACO. Dashed lines show the 95% completeness interval. The grey area represent the coronographic mask. Contrast curves provided by PCA and TLOCI do not strictly correspond to a 5σ false alarm rate contrarily to the contrast curves of PACO. The achievable contrasts are thus significantly over-optimistic for PCA and TLOCI (see discussion in the main text).

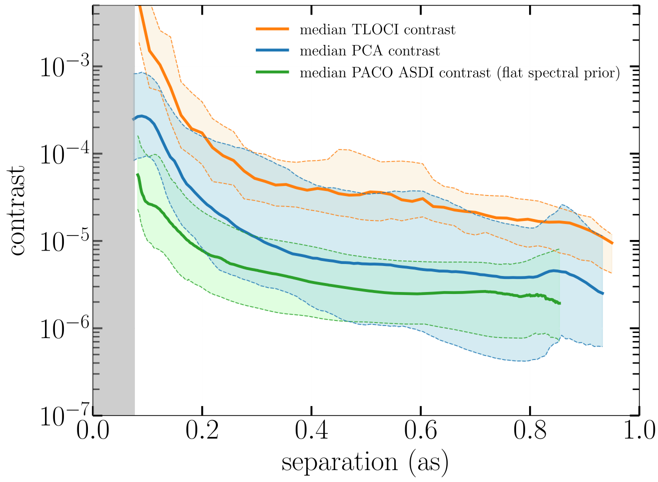

Fig. 10. Contrast comparison at 5σ between PACO, TLOCI, and PCA for IFS for the 24 science stars considered in this paper. Dashed lines show the 95% completeness interval. The grey area represents the coronographic mask. Contrast curves provided by PCA and TLOCI do not correspond to a 5σ false alarm rate contrarily to the contrast curves of PACO. The achievable contrasts are thus significantly over-optimistic for PCA and TLOCI (see discussion in the text).

comparison, we used the combined contrast of TLOCI and PCA, as well as the contrast obtained with the flat prior with PACO (hereafter noted as PACO-flat) to make the most direct comparison possible. Although it was not used in this study, we also included the median PACO ADI contrast curve (i.e., obtained without joint processing of the spectral channels) in Fig. 9 for reference. The gain offered by the ASDI mode is very close $\sqrt{2}$, which corresponds to the expected theoretical value when combining the information of two (independent) channels. In order to compare results from the three considered algorithms, it has to be noted that given the non-statistical nature of TLOCI and PCA, the 5σ detection limits are not statistically grounded; that is to say, we experienced in practice many more false alarms as theoretically expected for the targeted confidence level, especially at short angular separations from the target star. Moreover, the flat prior represents the most difficult case for PACO (especially for IFS) because we try to detect a signal with the same spectra as the host star, which means that the spectral prior does not explicitly help in disentangling the two components.

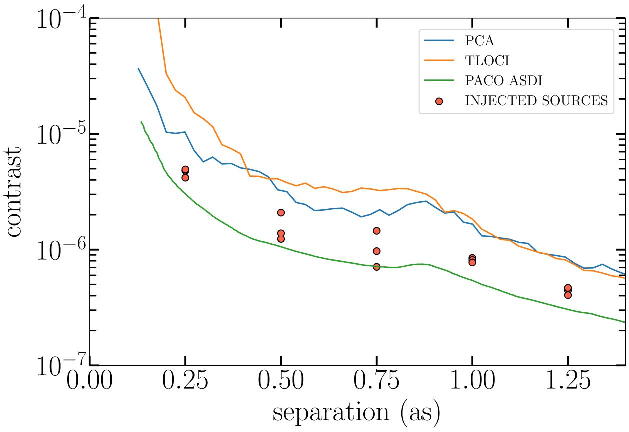

Fig. 11. Comparison of the contrast curves at 5σ obtained with PCA (5 modes), TLOCI, and PACO-flat for IRDIS on HD 377. The contrasts of the injected fake planets were computed using 2D contrast maps, thus, there are differences seen with the 5σ curve: local variations of the achieved contrast are averaged azimuthally.

For IRDIS, at close angular separations, PACO shows a better performance than TLOCI (resp. PCA) by a factor of about 7 (resp. 5) at 0.5″, and by 5 at 1″ and beyond compare to both TLOCI and PCA. Moreover, due to the statistical nature of PACO, the number of false positives follows what is expected at a 5σ confidence under a multivariate Gaussian hypothesis (see Fig. 6), unlike TLOCI and PCA.

For IFS, the gain ranges between a factor of 3 and 5, depending on the separation, compared to PCA. It is much larger compared to TLOCI by about a factor of 10 for all separations, but this result is expected as TLOCI performs worse on IFS as compared to PCA. However, the achieved performance in terms of contrast is much more consistent with PACO than it is with PCA. We remind that using the flat prior as a benchmark allows us to compare PACO with PCA/TLOCI as fairly as possible. It does not however represent the full capability of PACO to detect faint sources because this is the “worst” possible case, as we are trying to detect a highly correlated planetary spectrum with respect to the star spectrum.

5.2. Validation of the reliability of the contrast curves

Each algorithm uses different hypothesis to compute the contrast limits. To further assess the gain in contrast obtained with PACO, and the comparison with TLOCI or PCA, we present a set of numerical experiments. With PACO, the contrast is estimated assuming that the statistical parameters (mean and covariance matrices) characterizing the stellar leakages are computed from pure noise realizations. In practice, the underlying presence of the (unknown) sought objects corrupts these estimates, which leads to a (slight) bias in the estimated performance. In this section, we aim to quantify this bias via numerical experiments.

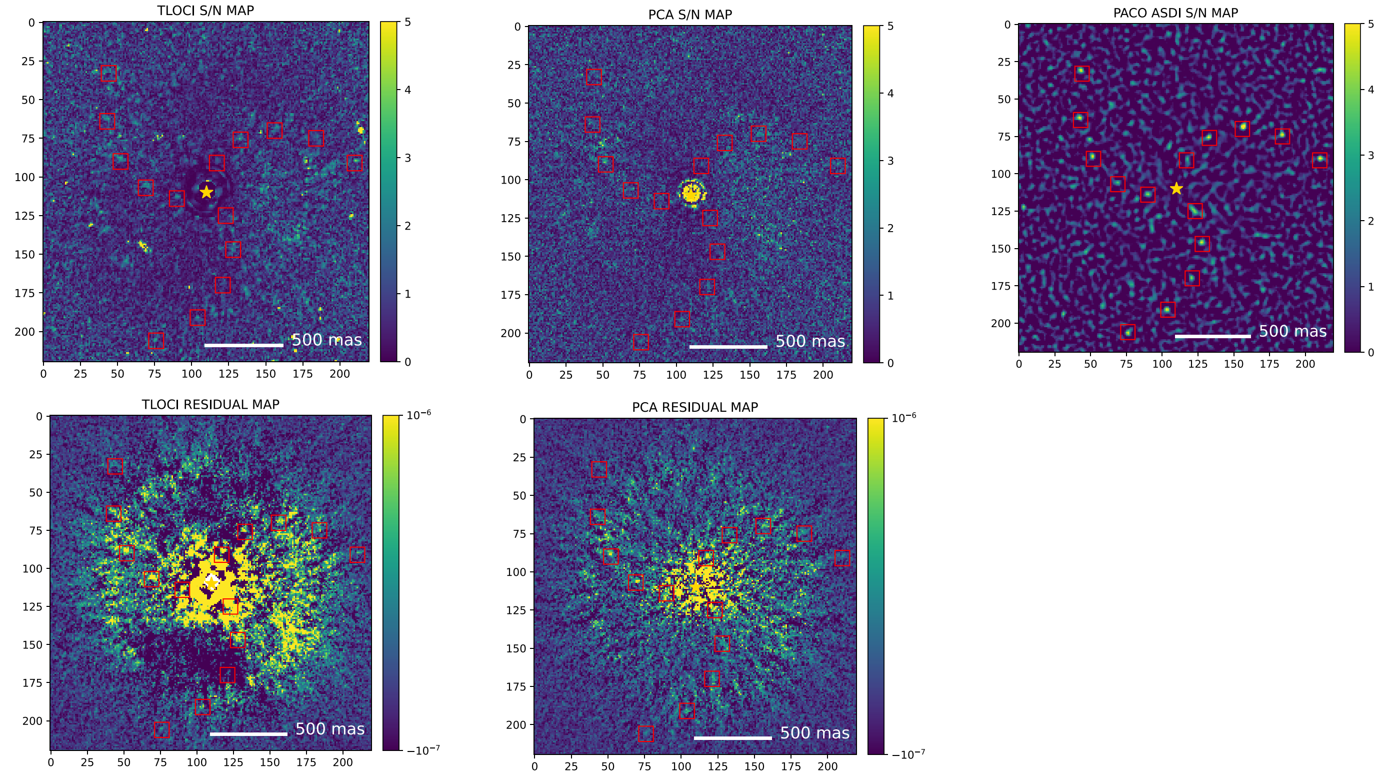

Fig. 12. S/N map provided by PACO (top right), residual map provided by SpeCal PCA using 10 modes (bottom middle), associated S/N map (top middle), residual map from TLOCI (bottom left) and associated S/N map (top left). The injected fake planets are clearly visible on the S/N maps from PACO. None of the high S/N detections on the PCA/TLOCI map corresponds to injected sources. The locations of injected sources are highlighted by the red boxes.

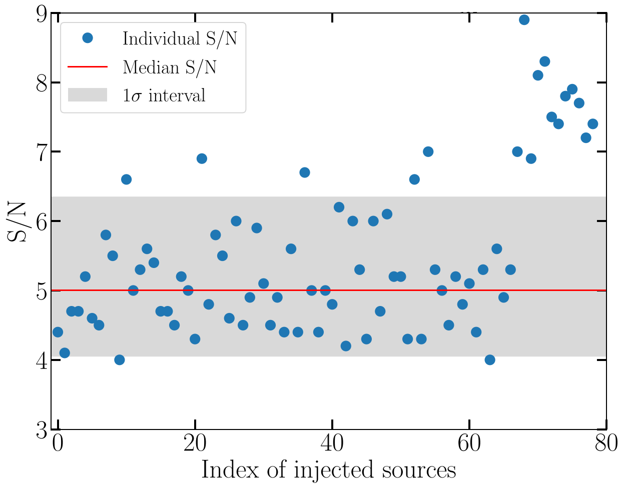

Fig. 13. Retrieved S/N for the injected sources for IRDIS. The detection threshold τ was set to 4. The red line shows the median S/N of the injected sources and the grey area the 1σ interval containing 68% of the detected injected sources.

For that purpose, we resorted to massive injections of FPSs at contrast levels predicted by PACO and we re-ran the algorithm to quantify the real detection confidence experienced for such levels of contrast. Ensuring such confidence is key to allow an unsupervised selection of candidate companions through simple thresholding of the derived S/N map. Given computational constraints, injection tests (as presented in Sects. 5.2.1 and 5.2.2) were performed on a dataset of HD 377 (star included in this study) for both IRDIS and IFS.

5.2.1. IRDIS data

For IRDIS, two sets were created: one with injections at close separations (<1.25 as) and one at large separations (>1.5 as), as described in Appendix B. For both, from the 2D contrast maps provided by PACO, we set the contrast of the FPSs in order to achieve (theoretically) a detection slightly above the 5σ threshold on the S/N map. More detailed information on the close-in injected sources parameters can be found in Table B.1. Figure 11 shows the injected sources contrast (red dots) compared to the contrast curve provided by PACO, as well as the contrast curves provided by TLOCI and PCA for this particular target in the first case (close separation). Figure 12 shows the S/N maps obtained with the three algorithms as well as residual maps[9] obtained after the subtraction of the estimated stellar component for PCA and TLOCI for the injections at close separations.

We also created a set of injections of companions at larger separations. Detailed information on the injected sources parameters can be found in Table B.2. Figure B.1 shows the contrast of the injected FPSs compared to the contrast curve of the three algorithms. The corresponding S/N and residual maps obtained after subtraction of the estimated stellar component for PCA and TLOCI are shown in Figs. B.2 to B.6.

Figure 13 shows the retrieved S/N of FPSs in both cases (for a total of 90 injected sources)[10]. The median S/N is 5.0 which is

---

[9] PACO does not produce residual maps since it describes the stellar component through a statistical model rather than resorting to explicit combinations and/or subtractions of images.

[10] Because we use a 4σ threshold for the analysis, we did not recover injections with a S/N below 4σ. We can however still find the median S/N by computing the S/N for which half of the injected sources (the 45 higher S/N sources in that case) have a higher S/N.

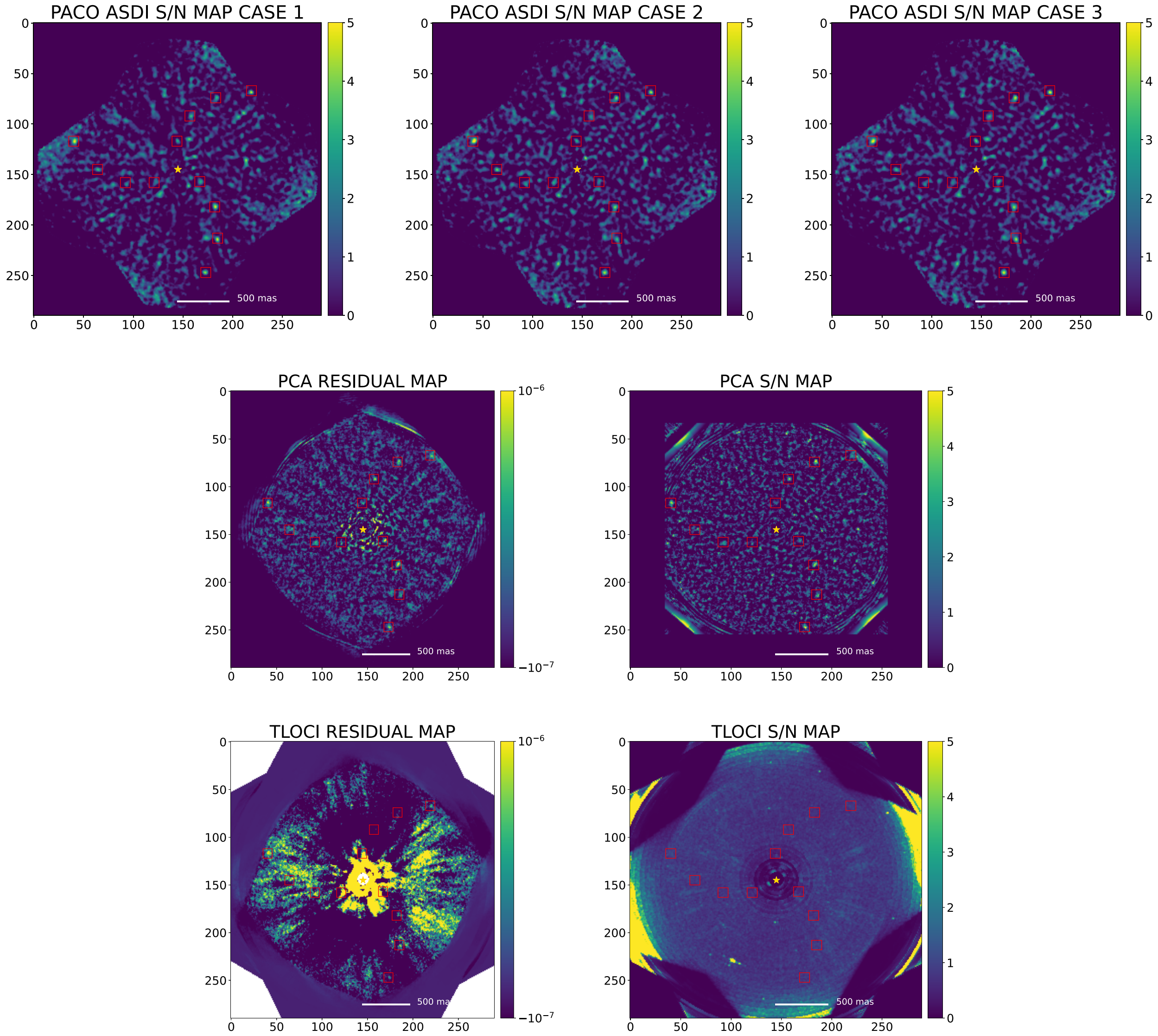

Fig. 14. S/N and residual maps for the injected fake sources on IFS. Top row: PACO ASDI S/N maps corresponding to the various injected spectra (see Fig. B.7). Middle row: Residual and S/N maps using PCA. Bottom row: Residual and S/N maps using TLOCI. The locations of injected sources are highlighted by red boxes.

Table 1. Properties of the signals detected in the IRDIS images.

EPOCH	SEP (mas)	PA (°)	M_{H2}	M_{H3}	S/N	STATUS
			HD 987			
2015-09-25	1133.0±2.1	42.3±0.1	17.73±0.23	17.78±0.23	11.9	BCKG
			HD 61005			
2015-02-02	5870.0±13.3	314.4±0.1	17.82±0.12	17.69±0.13	11.2	BCKG
2015-02-02	3046.0±7.1	327.0±0.1	17.88±0.13	17.86±0.13	11.1	BCKG

Notes. $M_{\mathrm{H2/3}}$ is the absolute magnitude of the candidate in both filters.

in very good agreement with the contrast of injection. We also calculated the empirical standard deviation value $\sigma = 1.15$. This result is also close to the theoretical value of 1 predicted by a Gaussian distribution.

These results confirm that the contrast estimates produced by PACO (e.g., shown in Fig. 9) are reliable and statistically grounded, and that the detection sensitivity is improved compared to TLOCI and PCA for the whole range of angular separations.

5.2.2. IFS data

For IFS, we injected 72 sources with three different shapes of spectra (24 sources per shape) corresponding to three of the spectral priors (flat, L-type, T-type) used during the reduction (hereafter denoted as cases), for which the contrast injected was also computed using the 2D contrast maps. We also considered a “flat” injection that corresponds (as the priors are expressed in contrast unit) to a SED with a same shape than that of the

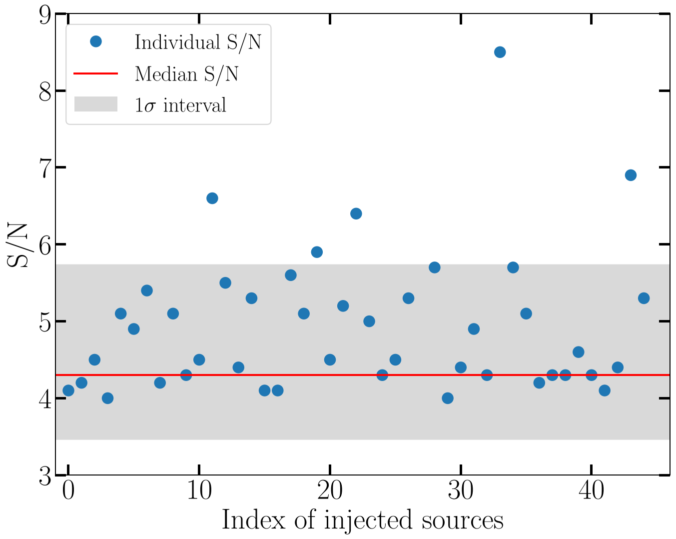

Fig. 15. Retrieved S/N for the injected sources for IFS. The detection threshold τ was set to 4. The red line shows the median S/N of the injected sources and the grey area the 1σ interval containing 68% of the detected injected sources.

star. The normalized spectra injected for the three cases can be found in Fig. B.7 as well as complete information on the injected sources in Table B.3. Corresponding S/N and residual maps are given in Fig. 14.

The S/N of the detected injections are shown in Fig. 15. As done for IRDIS, we can compute the median S/N of the injected sources, which is 4.3, with a standard deviation of 1.16. This suggests that the estimated contrast is slightly optimistic by about 15%.

As expected, we conclude that the detection limits in contrast derived by PACO for IFS are slightly optimistic without questioning the previously mentioned results, because the equivalent number of independent spectral channels that are recombined is about $L/2$. The detection sensitivity is still improved at all angular separation, coupled with the false positive rate consistent with the chosen S/N threshold.

6. Results of the mini-survey

6.1. Identified point sources and status

Running the PACO algorithm along with the analysis tools described in Sects. 4.2 and 4.4 over the 37 datasets of this survey allows us to identify 61 (58 IRDIS, 3 IFS) point-like sources with an S/N above the 5σ detection confidence. We note that one source, PZ TEL B, is detected with both instruments. For comparison, only 40 sources were detected by the F150 analysis. This again illustrates the enhanced detection capabilities of PACO with respect to more classical algorithms. We classify the sources as follows:

BCKG (background source): a source classified as background in the F150 or in this analysis using a proper motion analysis.

KC (known companion): either a planet, brown dwarf or stellar companion.

SUSP BCKG CMD (suspected background using a color magnitude diagram): source detected in the present analysis, which was not detected in the F150, with only one epoch available and a color consistent with a background nature.

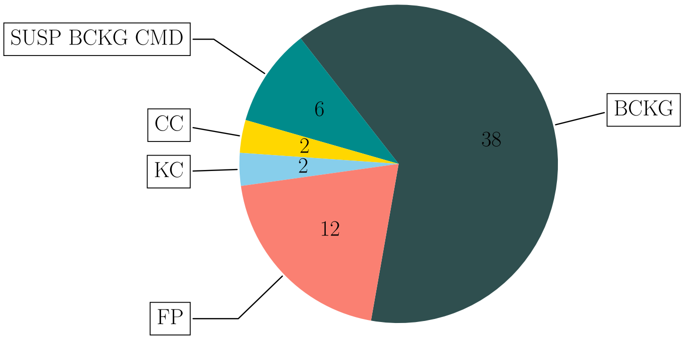

Fig. 16. Classification of the 60 sources detected during the survey. Note: PZ Tel B is visible in both IRDIS and IFS, thus accounted for only one source in this plot.

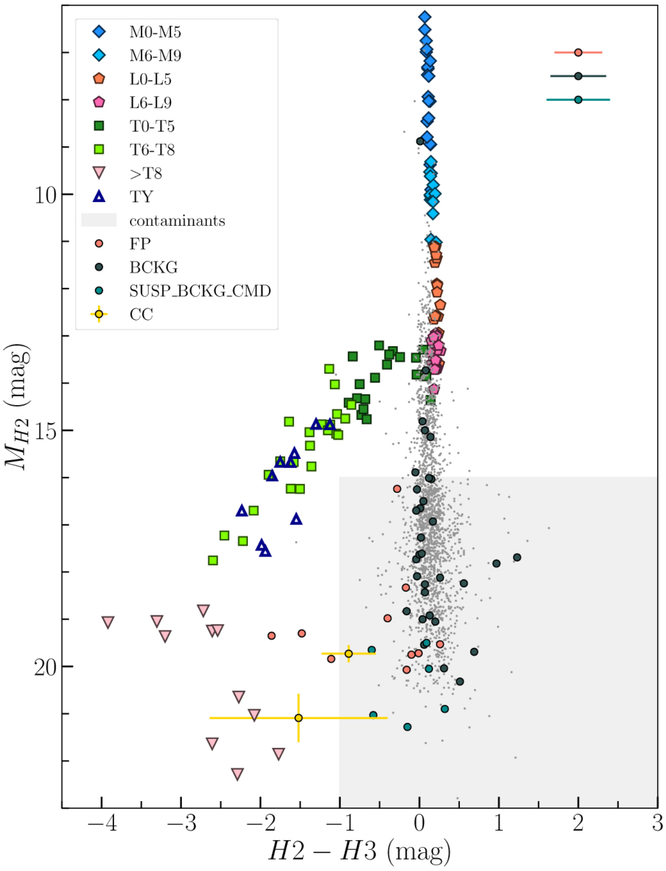

Fig. 17. CMD plot with the classification of the 60 sources detected during the survey. Note: individual error bars are not shown for clarity purposes except for the two most interesting candidates (yellow circles). Typical error bars are indicated in the top right. The grey dots represent the background sources identified during the SHINE F150 survey.

CC (candidate companion): a source detected in the present analysis that was not detected in the F150, with only one epoch and with a color compatible with a planetary or brown dwarf companion.

FP: a false positive identified using the multi-epoch tool described in Sect. 4.4. This classification is only possible for stars with multiple epochs with similar quality data.

Figure 16 shows a pie-chart diagram of the sources classification. Individual data are to be provided in a VizieR table (see Table 1 for an example of the parameters provided). Finally, the targets are plotted on a CMD in Fig. 17.

Among the 60 identified signal of interest, eight are not characterized because of a lack of a second epoch of observation.

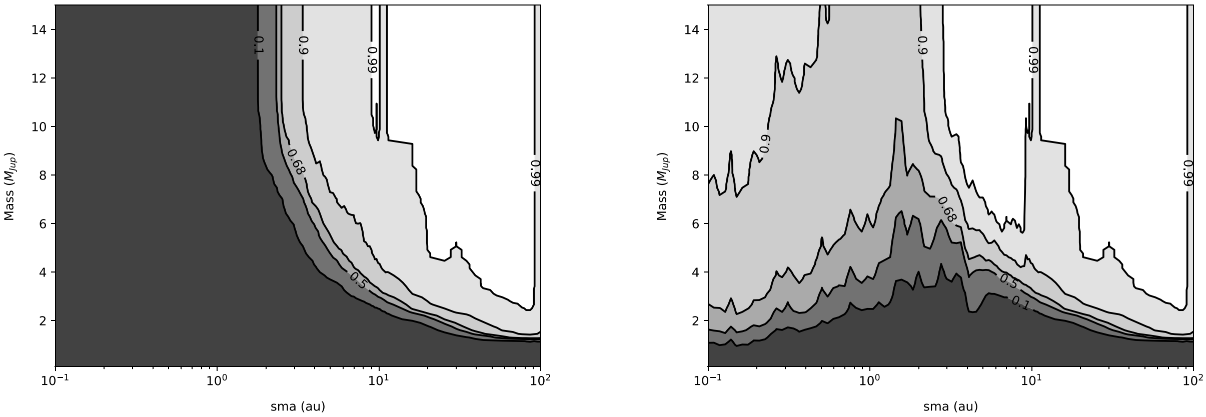

Fig. 18. Detection maps using the MESS2 (Lannier 2015) tool for HD 202917, DI only (left), DI+RV (right). The eccentricity is assumed between 0 and 0.5 and the inclination between 0 and 90 degrees. Contrast maps are converted to mass maps using the COND atmospheric model (Allard et al. 2001) and the stellar parameters of the system are extracted from Desidera et al. (2021). Two epochs were used here.

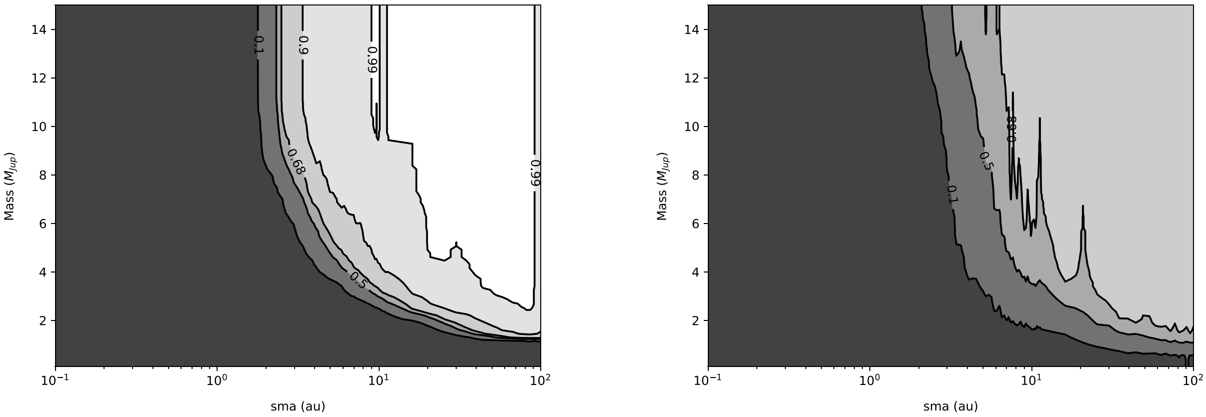

Fig. 19. Comparison between the detection limits obtained with PACO ASDI (left) and TLOCI (right) for HD 202917 using the MESS2 tool (Lannier 2015). The eccentricity is assumed between 0 and 0.5 and the inclination between 0 and 90 degrees. Contrast maps are converted to mass maps using the COND atmospheric model (Allard et al. 2001) and the stellar parameters of the system are extracted from Desidera et al. (2021). Two epochs were used.

Among those eight sources, six fall into the domain of probable background sources (grey area in Fig. 17). We classified them as SUSP BCKG CMD. Two are more promising giving their colors. They require additional observations to definitely distinguish between a background source, a false positive, or a bound companion. We therefore classified them as candidate companions (CC) at this stage.

Finally, we found twelve false positives over the course of this survey. Given the number of datasets for IRDIS (37) and the number of priors used (5), we should expect around 16 false positives (see Fig. 6). Taking also into account that FPs could be present amongst the eight sources classified as candidates companions (either “CC” or “SUSP BCKG CMD”), we conclude that this number is in good agreement with the theory predictions, confirming the Gaussian nature of noise in the detection maps of PACO. One IFS false positive was also found.

6.2. Searching for additional companions

Here, we want to put constraints on the properties of possible, yet unseen companions. We used the MESS2 tool (Lannier 2015) that uses, for each target, all the detection limit maps derived from the PACO analysis (expressed in terms of mass) as well as the radial velocity data, whenever they are available in the ESO HARPS (Mayor et al. 2003) archive. Indeed, the combination of direct imaging data with RV data provides a large exploration of the star’s environments, going from a fraction of au out to 100 au. To convert the PACO contrasts into detection limits expressed in masses, we use luminosity-mass relationships given by the COND atmospheric model (Allard et al. 2001), and the stars’ ages and masses provided by Desidera et al. (2021). Finally, to run MESS2, we assumed a uniform distribution of eccentricities between 0 and 0.5 and a uniform orbital plane inclination between 0 and 90 degrees.

An example of detection limits obtained using the imaging data alone, on the one hand, and using both the imaging and RV data, on the other hand, is provided in Fig. 18. The results obtained for all stars of the sample are presented in Appendix C.

The detection limits in terms of masses are significantly improved with respect to previous analyses, thanks to improved detection limits. For instance, we get a detection limit of about 5 M_{Jup} (68% probability) at 5 au for HD 202917, while the detection limit with TLOCI is 10 M_{Jup} at the same separation (see Fig. 19). At 10 au, 3 M_{Jup} planets could be detected, compared to 6 M_{Jup} with TLOCI. This represents a substantial improvement in the detection limits. Nonetheless, Jupiter siblings are still out of reach in the present data. Improved adaptive optics systems, such as that of the SPHERE+ project (Boccaletti et al. 2020) on the VLT, are needed to reach such objectives. Finally, we see that, in most cases, combining the radial velocity (RV) and direct imaging (DI) allows us to bridge the gap between the two techniques. The detection limits will be further improved using HIPPARCOS-*Gaia* data in the typical 3–10 au region.

7. Conclusion

Here, we present a number of upgrades made to our reduction and analysis pipeline using PACO that are aimed at improving the sensitivity and the characterization of the detected sources. In particular, we have improved the precision and robustness of the astrometric and photometric error bars for the detected sources. We have developed custom built spectral prior libraries to optimize the detection capability of the ASDI mode for both IRDIS and IFS. The contrast performances are significantly improved, compared to what can be obtained with classical algorithms such as TLOCI and PCA. Also, we have shown that PACO provides statistically meaningful S/N maps. This work paves the way toward an end-to-end, homogeneous, and unsupervised massive re-reduction of archival SPHERE direct imaging data in the quest for detecting exoJupiters.

We used PACO ASDI to search for exoJupiters in a sample of 24 selected young, solar-type targets observed with SPHERE IRDIS and IFS that are part of the SHINE survey. This new analysis allowed us to identify two candidate companions in this small sample. Second epochs are necessary to unveil their nature.

Acknowledgements. This project has also received funding from the European Research Council (ERC) under the European Union's Horizon 2020 research and innovation programme (COBREX; grant agreement no. 885593). SPHERE is an instrument designed and built by a consortium consisting of IPAG (Grenoble, France), MPIA (Heidelberg, Germany), LAM (Marseille, France), LESIA (Paris, France), Laboratoire Lagrange (Nice, France), INAF – Osservatorio di Padova (Italy), Observatoire de Genève (Switzerland), ETH Zürich (Switzerland), NOVA (Netherlands), ONERA (France) and ASTRON (Netherlands) in collaboration with ESO. SPHERE was funded by ESO, with additional contributions from CNRS (France), MPIA (Germany), INAF (Italy), FINES (Switzerland) and NOVA (Netherlands). SPHERE also received funding from the European Commission Sixth and Seventh Framework Programmes as part of the Optical Infrared Coordination Network for Astronomy (OPTICON) under grant number RII3-Ct-2004-001566 for FP6 (2004–2008), grant number 226604 for FP7 (2009–2012) and grant number 312430 for FP7 (2013–2016). This work has made use of the SPHERE Data Centre, jointly operated by OSUG/IPAG (Grenoble), PYTHEAS/LAM/CeSAM (Marseille), OCA/Lagrange (Nice), Observatoire de Paris/LESIA (Paris), and Observatoire de Lyon (OSUL/CRAL). This research has made use of the SIMBAD database and VizieR catalogue access tool, operated at CDS, Strasbourg, France. This work is supported by the French National Research Agency in the framework of the Investissements d'Avenir program (ANR-15-IDEX-02), through the funding of the "Origin of Life" project of the Univ. Grenoble-Alpes. This work was supported by the Action Spécifique Haute Résolution Angulaire (ASHRA) of CNRS/INSU co-funded by CNES. This work is based on observations collected at the European Southern Observatory under ESO programme(s) 096.C-0241(A/B/C/F/G), 095.C-0298(A/B/D/H), 1100.C-0481(F/G), 097.C-0865(A/B/C/D), 198.C-0209(A/E/G).

References

Allard, F. 2014, in Exploring the Formation and Evolution of Planetary Systems, 299, eds. M. Booth, B. C. Matthews, & J. R. Graham, 271
Allard, F., Hauschildt, P. H., Alexander, D. R., Tamanai, A., & Schweitzer, A. 2001, ApJ, 556, 357
Amara, A., & Quanz, S. P. 2012, MNRAS, 427, 948
Baudoz, P., Dorn, R. J., Lizon, J.-L., et al. 2010, SPIE Conf. Ser., 7735, 77355B
Beaulieu, J.-P., & Bachelet, E. 2021, in European Planetary Science Congress, EPSC2021-298
Beuzit, J.-L., Vigan, A., Mouillet, D., et al. 2019, A&A, 631, A155
Boccaletti, A., Chauvin, G., Mouillet, D., et al. 2020, arXiv e-prints [arXiv:`2003.05714`]
Branch, M. A., Coleman, T. F., & Li, Y. 1999, SIAM J. Sci. Comput., 21, 1
Charnay, B., Bézard, B., & Baudino, J.-L. 2019, in EPSC-DPS Joint Meeting 2019, 2019, EPSC-DPS2019-1450
Childs, A. C., Quintana, E., Barclay, T., & Steffen, J. H. 2019, MNRAS, 485, 541
Claudi, R. U., Turatto, M., Gratton, R. G., et al. 2008, SPIE Conf. Ser., 7014, 70143E
Dallant, J., Langlois, M., & Flasseur, O. 2023, A&A, submitted
Delorme, P., Meunier, N., Albert, D., et al. 2017, in SF2A-2017: Proceedings of the Annual Meeting of the French Society of Astronomy and Astrophysics, eds. C. Reylé, P. Di Matteo, F. Herpin, et al.
Desidera, S., Chauvin, G., Bonavita, M., et al. 2021, A&A, 651, A70
Dohlen, K., Langlois, M., Saisse, M., et al. 2008, SPIE Conf. Ser., 7014, 70143L
Fernandes, R. B., Mulders, G. D., Pascucci, I., Mordasini, C., & Emsenhuber, A. 2019, ApJ, 874, 81
Flasseur, O., Denis, L., Thiébaut, É., & Langlois, M. 2018, A&A, 618, A138
Flasseur, O., Denis, L., Thiébaut, É., & Langlois, M. 2020a, A&A, 637, A9
Flasseur, O., Denis, L., Thiébaut, É., & Langlois, M. 2020b, A&A, 634, A2
Fulton, B. J., Rosenthal, L. J., Hirsch, L. A., et al. 2021, ApJS, 255, 14
Galicher, R., Boccaletti, A., Mesa, D., et al. 2018, A&A, 615, A92
Horner, J., & Jones, B. W. 2010, Astron. Geophys., 51, 6.16
Huber, P. J. 2011, in International Encyclopedia of Statistical Science (Springer), 1248
Lagrange, A. M., Philipot, F., Rubini, P., et al. 2023, A&A, accepted [arXiv:`2305.00047`]
Langlois, M., Gratton, R., Lagrange, A. M., et al. 2021, A&A, 651, A71
Lannier, J. 2015, in IAU General Assembly, 29, 2255268
Lannier, J., Lagrange, A. M., Bonavita, M., et al. 2017, A&A, 603, A54
Levison, H. F., & Agnor, C. 2003, AJ, 125, 2692
Macintosh, B., Gemini Planet Imager instrument Team, Planet Imager Exoplanet Survey, G., & Observatory, G. 2014, American Astronomical Society Meeting Abstracts #223, 229.02
Maire, A.-L., Langlois, M., Delorme, P., et al. 2021, J. Astron. Telescopes Instrum. Syst., 7, 035004
Maréchal, A. 1948, Étude des effets combinés de la diffraction et des aberrations géométriques sur l'image d'un point lumineux... (Éditions de la Revue d'optique théorique et instrumentale)
Marois, C., Lafrenière, D., Doyon, R., Macintosh, B., & Nadeau, D. 2006, ApJ, 641, 556
Marois, C., Correia, C., Véran, J.-P., & Currie, T. 2014, in Exploring the Formation and Evolution of Planetary Systems, 299, eds. M. Booth, B. C. Matthews, & J. R. Graham, 48
Mayor, M., Pepe, F., Queloz, D., et al. 2003, The Messenger, 114, 20
Mesa, D., Gratton, R., Zurlo, A., et al. 2015, A&A, 576, A121
Meunier, N., & Lagrange, A. M. 2019, A&A, 629, A42
Milli, J., Hibon, P., Christiaens, V., et al. 2017, A&A, 597, A2
Morbidelli, A., Lunine, J. I., O'Brien, D. P., Raymond, S. N., & Walsh, K. J. 2012, Annu. Rev. Earth Planet. Sci., 40, 251
Perryman, M., Hartman, J., Bakos, G. Á., & Lindegren, L. 2014, ApJ, 797, 14
Quintana, E. V., & Barclay, T. 2016, in American Astronomical Society Meeting Abstracts, #228, 404.05
Ranalli, P., Hobbs, D., & Lindegren, L. 2018, A&A, 614, A30
Raymond, S. N., Kokubo, E., Morbidelli, A., Morishima, R., & Walsh, K. J. 2014, in Protostars and Planets VI, eds. H. Beuther, R. S. Klessen, C. P. Dullemond, & T. Henning, 595
Soummer, R., Pueyo, L., & Larkin, J. 2012, ApJ, 755, L28
Suárez Valles, M., Fedrigo, E., Donaldson, R. H., et al. 2012, SPIE Conf. Ser., 8447, 84472Q
Vigan, A., Fontanive, C., Meyer, M., et al. 2021, A&A, 651, A72
Wittenmyer, R. A., Butler, R. P., Wang, L., et al. 2016, MNRAS, 455, 1398

Appendix A: Target parameters and observing logs

NAME	OTHER ID	RA^a	DEC^a	H (mag)	dist (pc)^b	age (Myr)^c	ST^d	MG^e
BD-12 243	-	01 20 32.2680	-11 28 03.727	6.65	35.3	149^{+31}_{-49}	G9V	ABDO
CD-31 16041	-	18 50 44.4830	-31 47 47.382	7.67	49.5	24^{+5}_{-5}	K8Ve	BPIC
CD-61 1439	-	06 39 50.0234	-61 28 41.530	6.64	22.2	149^{+31}_{-49}	K7V(e)	ABDO
HD105	-	00 05 52.5447	-41 45 11.044	6.19	38.8	45^{+5}_{-10}	G0V	TUC
HD118100	-	13 34 43.2063	-08 20 31.338	6.31	20.5	150^{+50}_{-50}	K5Ve	-
HD1466	-	00 18 26.1235	-63 28 38.980	6.25	42.8	45^{+5}_{-10}	F8V	TUC
HD164249	-	18 03 03.4097	-51 38 56.432	6.02	49.3	24^{+5}_{-5}	F6V	BPIC
HD174429	V*PZTel	18 53 05.8735	-50 10 49.897	6.49	47.3	24^{+5}_{-5}	G9IV	BPIC
HD17925	-	02 52 32.1281	-12 46 10.968	4.13	10.4	150^{+150}_{-80}	K1V	-
HD181327	-	19 22 58.9437	-54 32 16.975	5.98	47.8	24^{+5}_{-5}	F6V	BPIC
HD189245	-	20 00 20.2493	-33 42 12.424	4.64	22.1	150^{+150}_{-70}	F7V	-
HD197890	V*BOMic	20 47 45.0056	-36 35 40.769	6.93	51.0	45^{+55}_{-35}	K3V(e)	-
HD202917	-	21 20 49.9576	-53 02 03.155	7.03	46.7	45^{+5}_{-10}	G7V	TUC
HD218860	-	23 11 52.0534	-45 08 10.631	7.11	47.8	149^{+31}_{-49}	G8V	ABDO
HD224228	-	23 56 10.6732	-39 03 08.409	6.01	22.0	149^{+31}_{-49}	K2V	ABDO
HD377	-	00 08 25.7454	+06 37 00.489	6.15	38.4	150^{+50}_{-50}	G2V	-
HD43989	V*V1358Ori	06 19 08.0574	-03 26 20.361	6.59	51.7	42^{+8}_{-7}	G0V	TUC
HD44627	-	06 19 12.9130	-58 03 15.527	7.09	50.1	45^{+5}_{-10}	K1V(e)	CAR
HD45270	-	06 22 30.9408	-60 13 07.147	5.16	23.9	149^{+31}_{-49}	G1V	ABDO
HD49855	-	06 43 46.2456	-71 58 35.390	7.38	55.4	45^{+5}_{-10}	G6V	CAR
HD61005	-	07 35 47.4623	-32 12 14.045	6.58	36.5	50^{+20}_{-10}	G8Vk	-
HD8558	-	01 23 21.2547	-57 28 50.688	6.95	45.3	45^{+5}_{-10}	G7V	TUC
HD90712	-	10 27 47.7769	-34 23 58.130	6.15	37.7	150^{+50}_{-80}	G0V	-
HD987	-	00 13 53.0108	-74 41 17.850	7.09	45.9	45^{+5}_{-10}	G8V	TUC

Table A.1: Summary of the main parameters of the targeted stars.

Notes: ^{a}: Coordinates in J2000 IRCS. ^{b}: Distances as derived from the parallaxes provided by Simbad. ^{c}: Ages as extracted from Desidera et al. (2021). ^{d}: Spectral type. ^{e}: Moving group.

STAR	DATE OBS	FILTER	DIT(s)×Nframe	ΔPA (°)^a	Seeing (")^b	Airmass^b	τ_0 (ms)^{a,b}	Program ID
BD-12 243	2015-12-01	DB_H23	64x64	51.0	1.1	1.04	7	096.C-0241(B)
BD-12 243	2015-12-01	OBS_YJ	64x64	51.1	1.1	1.04	7	096.C-0241(B)
CD-31 16041	2015-05-15	DB_H23	64x64	81.2	1.1	1.02	3.4	095.C-0298(A)
CD-31 16041	2015-05-15	OBS_YJ	64x64	81.3	1.08	1.02	3.4	095.C-0298(A)
CD-31 16041	2018-04-17	DB_H23	96x42	84.5	0.88	1.01	10.3	1100.C-0481(F)
CD-31 16041	2018-04-17	OBS_YJ	96x42	83.8	0.88	1.01	10.3	1100.C-0481(F)
CD-61 1439	2016-01-02	DB_H23	64x64	26.1	0.9	1.25	2.4	096.C-0241(C)
CD-61 1439	2016-01-02	OBS_YJ	64x64	26.1	0.91	1.25	2.4	096.C-0241(C)
HD105	2015-09-26	DB_H23	64x72	45.0	1.06	1.07	17.4	095.C-0298(D)
HD105	2015-09-26	OBS_YJ	64x68	109.9	0.98	1.07	17.4	095.C-0298(D)
HD118100	2016-06-27	DB_H23	64x64	52.0	0.8	1.05	3.8	097.C-0865(C)
HD1466	2015-10-26	DB_H23	64x64	25.0	1.07	1.29	1.4	096.C-0241(A)
HD1466	2015-10-26	OBS_YJ	64x64	25.1	1.08	1.29	1.4	096.C-0241(A)
HD1466	2016-09-18	DB_H23	64x80	31.1	0.8	1.29	4.9	097.C-0865(D)
HD1466	2016-09-18	OBS_YJ	64x80	31.3	0.8	1.29	4.9	097.C-0865(D)
HD164249	2015-05-10	DB_H23	64x56	34.3	1.87	1.13	1.2	095.C-0298(A)
HD164249	2015-05-10	OBS_YJ	64x56	34.5	1.86	1.13	1.2	095.C-0298(A)
HD164249	2015-06-01	DB_H23	64x64	33.9	1.24	1.13	1.1	095.C-0298(B)
HD164249	2015-06-01	OBS_YJ	64x64	34.1	1.25	1.13	1.1	095.C-0298(B)
HD164249	2016-04-17	DB_H23	64x61	37.3	1.72	1.13	1.5	097.C-0865(A)
HD164249	2016-04-17	OBS_YJ	64x61	37.3	1.72	1.13	1.5	097.C-0865(A)
HD164249	2018-04-11	DB_H23	96x40	31.9	0.52	1.13	5.6	1100.C-0481(F)
HD164249	2018-04-11	OBS_YJ	96x40	32.0	0.52	1.13	5.6	1100.C-0481(F)
HD174429	2015-05-06	DB_H23	16x82	11.4	1.43	1.14	1.3	095.C-0298(A)
HD174429	2015-05-06	OBS_YJ	32x2	0.3	1.43	1.14	1.3	095.C-0298(A)
HD174429	2015-05-31	DB_H23	32x32	9.3	1.28	1.11	1	095.C-0298(B)
HD174429	2015-05-31	OBS_YJ	32x32	9.3	1.28	1.11	1	095.C-0298(B)
HD174429	2016-09-17	DB_H23	32x80	29.0	0.56	1.11	14.3	097.C-0865(D)
HD174429	2016-09-17	OBS_YJ	64x40	28.8	0.56	1.11	14.3	097.C-0865(D)
HD174429	2017-05-18	DB_H23	32x60	33.1	0.81	1.11	2.8	198.C-0209(G)
HD174429	2017-05-18	OBS_YJ	64x57	36.8	0.81	1.11	2.8	198.C-0209(G)

HD174429	2018-05-13	DB_H23	16x30	8.9	0.81	1.12	3.4	1100.C-0481(G)
HD174429	2018-05-13	OBS_YJ	32x30	9.5	0.85	1.12	3.4	1100.C-0481(G)
HD17925	2016-10-15	DB_H23	32x160	70.8	0.66	1.03	2.5	198.C-0209(A)
HD17925	2016-10-15	OBS_YJ	64x80	70.0	0.66	1.03	2.5	198.C-0209(A)
HD181327	2015-05-10	DB_H23	64x56	31.1	1.2	1.16	1.7	095.C-0298(A)
HD181327	2015-05-10	OBS_YJ	64x52	31.2	1.2	1.16	1.7	095.C-0298(A)
HD189245	2015-05-14	DB_H23	32x128	16.2	0.75	1.13	6.9	095.C-0298(A)
HD189245	2015-05-14	OBS_YJ	32x128	18.2	0.73	1.13	6.9	095.C-0298(A)
HD197890	2015-06-04	DB_H23	64x64	61.5	1.25	1.03	2.9	095.C-0298(B)
HD197890	2015-06-04	OBS_YJ	64x64	62.4	1.23	1.03	2.9	095.C-0298(B)
HD202917	2015-05-31	DB_H23	64x86	49.6	1.25	1.15	1.1	095.C-0298(B)
HD202917	2015-05-31	OBS_YJ	64x64	32.8	1.44	1.14	0.9	095.C-0298(B)
HD202917	2016-05-31	DB_H23	64x64	32.7	0.83	1.14	2.6	097.C-0865(B)
HD202917	2016-05-31	OBS_YJ	64x64	32.8	0.84	1.14	2.6	097.C-0865(B)
HD218860	2015-09-30	DB_H23	64x64	43.8	0.68	1.07	3.9	095.C-0298(D)
HD218860	2015-09-30	OBS_YJ	64x64	44.1	0.7	1.07	3.9	095.C-0298(D)
HD224228	2015-10-25	DB_H23	64x64	59.3	1.48	1.04	1.1	096.C-0241(A)
HD224228	2015-10-25	OBS_YJ	64x64	59.4	1.51	1.04	1.1	096.C-0241(A)
HD377	2016-10-14	DB_H23	64x80	35.8	0.63	1.18	2.8	198.C-0209(A)
HD377	2016-10-14	OBS_YJ	64x80	35.9	0.62	1.18	2.8	198.C-0209(A)
HD43989	2015-10-28	DB_H23	64x80	48.5	1.01	1.08	1.9	096.C-0241(F)
HD43989	2015-10-28	OBS_YJ	64x80	48.3	1.0	1.08	1.9	096.C-0241(F)
HD43989	2017-02-09	DB_H23	64x56	36.5	0.63	1.09	8.7	198.C-0209(E)
HD43989	2017-02-09	OBS_YJ	64x56	36.4	0.62	1.09	8.7	198.C-0209(E)
HD44627	2015-02-06	DB_H23	64x64	28.3	1.08	1.2	5.3	095.C-0298(H)
HD44627	2015-02-06	OBS_YJ	64x64	28.4	1.07	1.2	5.3	095.C-0298(H)
HD45270	2016-01-16	DB_H23	16x256	28.3	1.69	1.23	1.6	096.C-0241(G)
HD45270	2016-01-16	OBS_YJ	64x64	27.2	1.73	1.23	1.5	096.C-0241(G)

Table A.2: Star sample observation logs.

Notes: ^{a}: DIT correspond to the detector integration time per frame, ΔPA is the amplitude of the parallactic rotation, τ_0 corresponds to the coherence time. ^{b}: Values extracted from the updated DIMM info and averaged over the sequence.

STAR	DATE OBS	FILTER	DIT(s)×Nframe	ΔPA (°)^a	Seeing (")^b	Airmass^b	τ_0 (ms)^{a,b}	Program ID
HD49855	2015-12-28	DB_H23	64x64	21.4	0.84	1.48	2.9	096.C-0241(C)
HD49855	2015-12-28	OBS_YJ	64x64	21.5	0.83	1.48	2.9	096.C-0241(C)
HD61005	2015-02-03	DB_NDH23	64x64	93.0	0.66	1.01	23.1	095.C-0298(H)
HD61005	2015-02-03	OBS_YJ	64x66	96.9	0.67	1.01	23.1	095.C-0298(H)
HD8558	2015-09-24	DB_H23	64x64	28.8	2.05	1.19	0.9	095.C-0298(D)
HD8558	2015-09-24	OBS_YJ	64x64	28.9	2.05	1.19	0.9	095.C-0298(D)
HD8558	2015-10-28	DB_H23	64x64	28.2	1.02	1.2	2	096.C-0241(A)
HD8558	2015-10-28	OBS_YJ	64x64	28.4	1.02	1.2	2	096.C-0241(A)
HD8558	2016-10-14	DB_H23	64x64	28.2	0.56	1.2	2.8	198.C-0209(A)
HD8558	2016-10-14	OBS_YJ	64x64	28.3	0.56	1.2	2.8	198.C-0209(A)
HD90712	2016-01-03	DB_H23	64x64	74.8	0.67	1.02	6.1	096.C-0241(C)
HD90712	2016-01-03	OBS_YJ	64x64	74.9	0.65	1.02	6.1	096.C-0241(C)
HD987	2016-10-15	DB_H23	64x90	29.7	0.71	1.56	2.2	198.C-0209(A)
HD987	2016-10-15	OBS_YJ	64x90	29.7	0.71	1.56	2.2	198.C-0209(A)

Table A.3: Star sample observation logs (continuation of Table A.2).

Notes: ^{a}: DIT corresponds to the detector integration time per frame, ΔPA is the amplitude of the parallactic rotation, τ_0 corresponds to the coherence time. ^{b}: Values extracted from the updated DIMM info and averaged over the sequence.

NAME	OTHER ID	RA^a	DEC^a	H (mag)	dist (pc)^b	age (Myr)^c	ST
Smethells86	-	21 44 30.1227	-60 58 38.894	8.09	46.4	45^{+5}_{-10}	M0Ve
V*CT Tuc	-	00 25 14.6618	-61 30 48.252	7.94	44.1	45^{+5}_{-10}	M0Ve
HD108767B	*delCrvB	12 29 50.8908	-16 31 15.208	6.37	26.8	180^{+170}_{-80}	K1
HD16978	*epsHyi	02 39 35.3612	-68 16 01.010	4.43	46.6	45^{+5}_{-10}	B9Va

Table A.4: Summary of the main parameters of the test stars

Notes: ^{a}: Coordinates in J2000 IRCS. ^{b}: Distances derived from Simbad parallaxes. ^{c}: Age extracted from Desidera et al. (2021). ^{d}: Spectral type.

STAR	DATE OBS	FILTER	DIT(s)×Nframe	ΔPA (°)[a]	Seeing (")[b]	Airmass[b]	τ_0 (ms)[a,b]	Program ID
V*CT Tuc	2015-07-05	DB_H23	64x64	26.0	1.07	1.25	2	095.C-0298(C)
V*CTTuc	2015-07-05	OBS_YJ	64x64	26.2	1.07	1.25	2	095.C-0298(C)
Smethells 86	2015-11-29	DB_H23	64x64	25.8	1.57	1.26	7.2	096.C-0241(B)
Smethells 86	2015-11-29	OBS_YJ	64x64	25.8	1.57	1.26	7.2	096.C-0241(B)
HD108767B	2018-01-25	DB_H23	64x72	94.4	0.59	1.02	8.3	1100.C-0481(D)
HD108767B	2018-01-25	OBS_YJ	64x72	94.3	0.59	1.02	8.3	1100.C-0481(D)
HD16978	2016-09-16	DB_H23	32x160	29.1	0.42	1.38	9.2	097.C-0865(D)
HD16978	2016-09-16	OBS_YJ	32x144	26.8	0.42	1.38	9.2	097.C-0865(D)

Table A.5: Test targets observation logs.

Notes: [a]: DIT corresponds to the detector integration time per frame, ΔPA is the amplitude of the parallactic rotation, τ_0 corresponds to the coherence time. [b]: Values extracted from the updated DIMM info and averaged over the sequence.

Appendix B: Compared detection and contrast maps between PACO ASDI, TLOCI and PCA for 5σ injected sources from PACO detection limits

SEP (mas)	PA (°)	CONTRAST	SEP (mas)	PA (°)	CONTRAST	SEP (mas)	PA (°)	CONTRAST
250	100	4.81×10^{-6}	250	220	4.18×10^{-6}	250	340	4.92×10^{-6}
500	85	2.09×10^{-6}	500	205	1.24×10^{-6}	500	325	1.38×10^{-6}
750	70	1.45×10^{-6}	750	190	7.12×10^{-7}	750	310	9.73×10^{-7}
1000	55	8.46×10^{-7}	1000	175	8.10×10^{-7}	1000	295	7.78×10^{-7}
1250	40	4.44×10^{-7}	12500	160	4.05×10^{-7}	1250	280	4.68×10^{-7}

Table B.1: IRDIS injected fake planets parameters.

SEP (mas)	PA (°)	CONTRAST	SEP (mas)	PA (°)	CONTRAST	SEP (mas)	PA (°)	CONTRAST
1500	100	3.07×10^{-7}	1500	160	3.20×10^{-7}	1500	220	3.08×10^{-7}
1500	280	2.87×10^{-7}	1500	340	3.18×10^{-7}	1750	85	2.51×10^{-7}
1750	145	2.57×10^{-7}	1750	205	2.44×10^{-7}	1750	265	2.43×10^{-7}
1750	325	2.50×10^{-7}	2000	70	2.24×10^{-7}	2000	130	2.07×10^{-7}
2000	190	2.19×10^{-7}	2000	250	2.15×10^{-7}	2000	310	2.19×10^{-7}
2250	55	2.10×10^{-7}	2250	115	1.93×10^{-7}	2250	175	2.12×10^{-7}
2250	235	2.16×10^{-7}	2250	295	1.96×10^{-7}	2500	40	1.94×10^{-7}
2500	100	1.89×10^{-7}	2500	160	1.92×10^{-7}	2500	220	1.96×10^{-7}
2500	280	1.88×10^{-7}	2750	25	1.91×10^{-7}	2750	85	1.89×10^{-7}
2750	145	1.73×10^{-7}	2750	205	1.91×10^{-7}	2750	265	1.87×10^{-7}
3000	10	1.72×10^{-7}	3000	70	1.81×10^{-7}	3000	130	1.66×10^{-7}
3000	190	1.78×10^{-7}	3000	250	1.77×10^{-7}	3250	355	1.71×10^{-7}
3250	55	1.68×10^{-7}	3250	115	1.87×10^{-7}	3250	175	1.79×10^{-7}
3250	235	1.76×10^{-7}	3500	340	1.66×10^{-7}	3500	40	1.71×10^{-7}
3500	100	1.68×10^{-7}	3500	160	1.76×10^{-7}	3500	220	1.72×10^{-7}
3750	325	1.68×10^{-7}	3750	25	1.76×10^{-7}	3750	85	1.67×10^{-7}
3750	145	1.72×10^{-7}	3750	205	1.85×10^{-7}	4000	310	1.74×10^{-7}
4000	10	1.76×10^{-7}	4000	70	1.80×10^{-7}	4000	130	1.71×10^{-7}
4000	190	1.74×10^{-7}	4250	295	1.72×10^{-7}	4250	355	1.63×10^{-7}
4250	55	1.73×10^{-7}	4250	115	1.64×10^{-7}	4250	175	1.80×10^{-7}
4500	280	1.69×10^{-7}	4500	340	1.74×10^{-7}	4500	40	1.63×10^{-7}
4500	100	1.71×10^{-7}	4500	160	1.69×10^{-7}	4750	265	1.69×10^{-7}
4750	325	1.65×10^{-7}	4750	25	1.63×10^{-7}	4750	85	1.66×10^{-7}
4750	145	1.65×10^{-7}	5000	190	1.65×10^{-7}	5000	250	1.87×10^{-7}
5000	10	1.69×10^{-7}	5000	70	1.73×10^{-7}	5000	130	1.64×10^{-7}

Table B.2: IRDIS injected fake planets parameters.

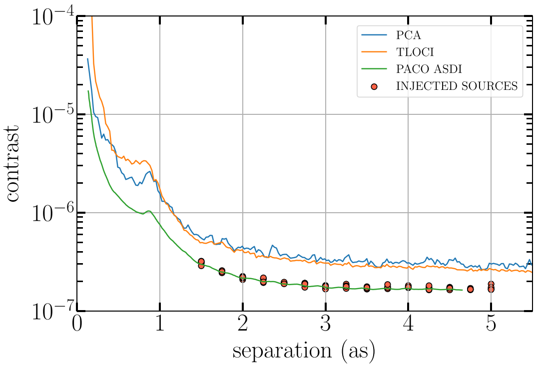

Fig. B.1: Contrast comparison between PCA (10 modes), TLOCI and PACO. The contrast of the injected fake planets were computed using 2D contrast maps, hence, we can see the differences with the 5σ curve: local variations of the achieved contrast are averaged azimuthally.

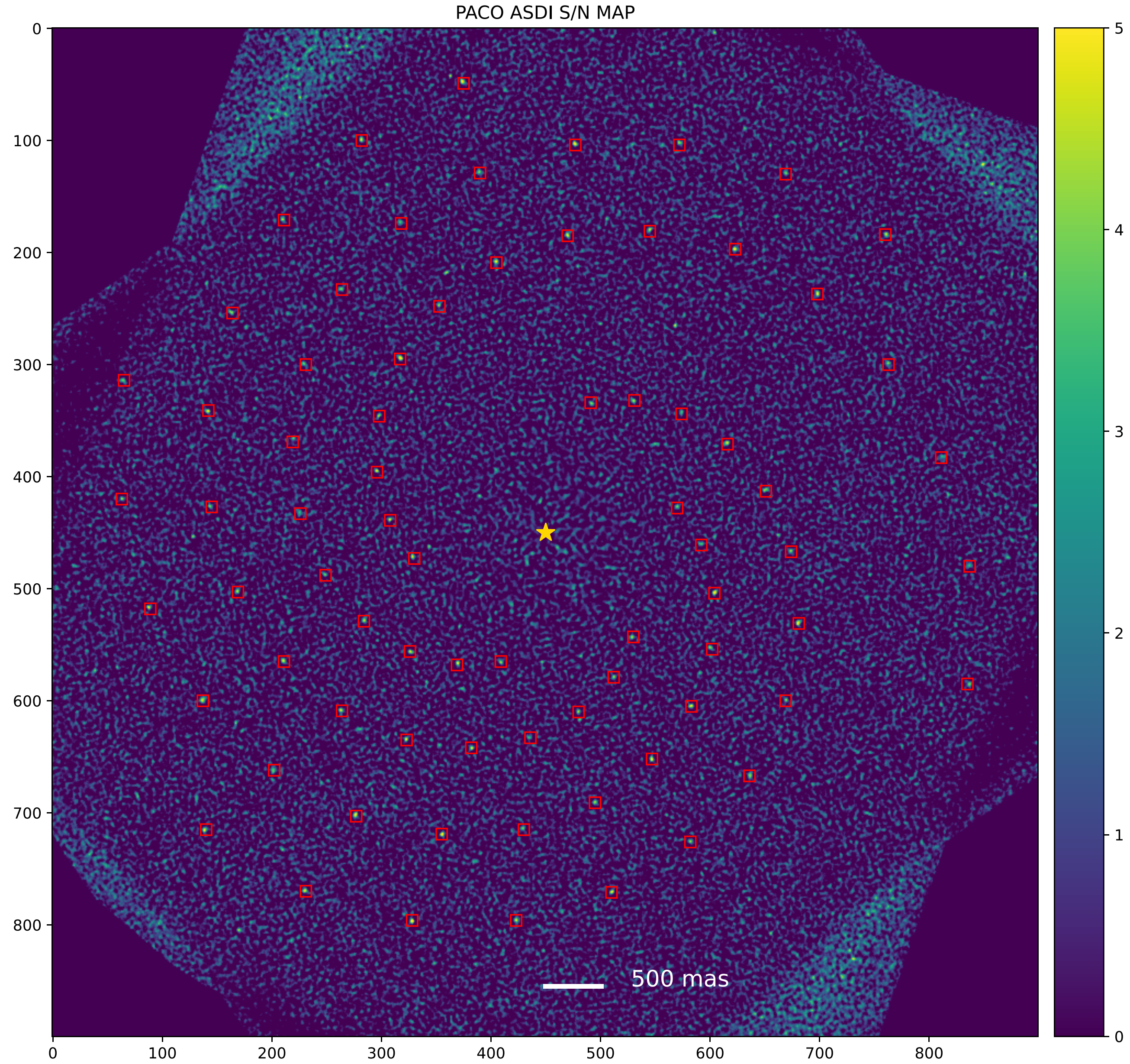

Fig. B.2: PACO ASDI S/N map assuming the SED of sought sources is flat. The locations of injected sources are highlighted by the red boxes.

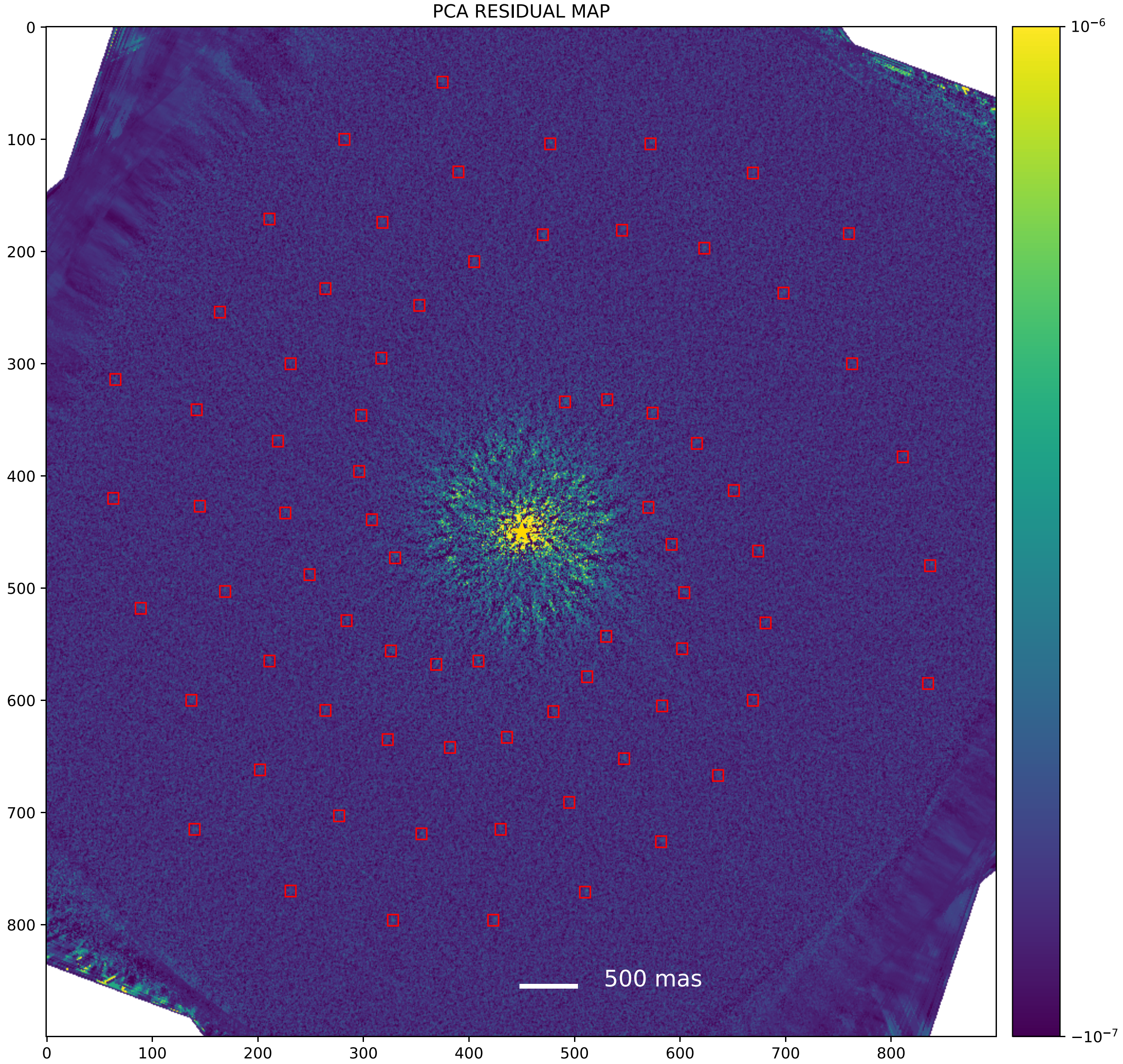

Fig. B.3: PCA residual map. The locations of injected sources are highlighted by red boxes.

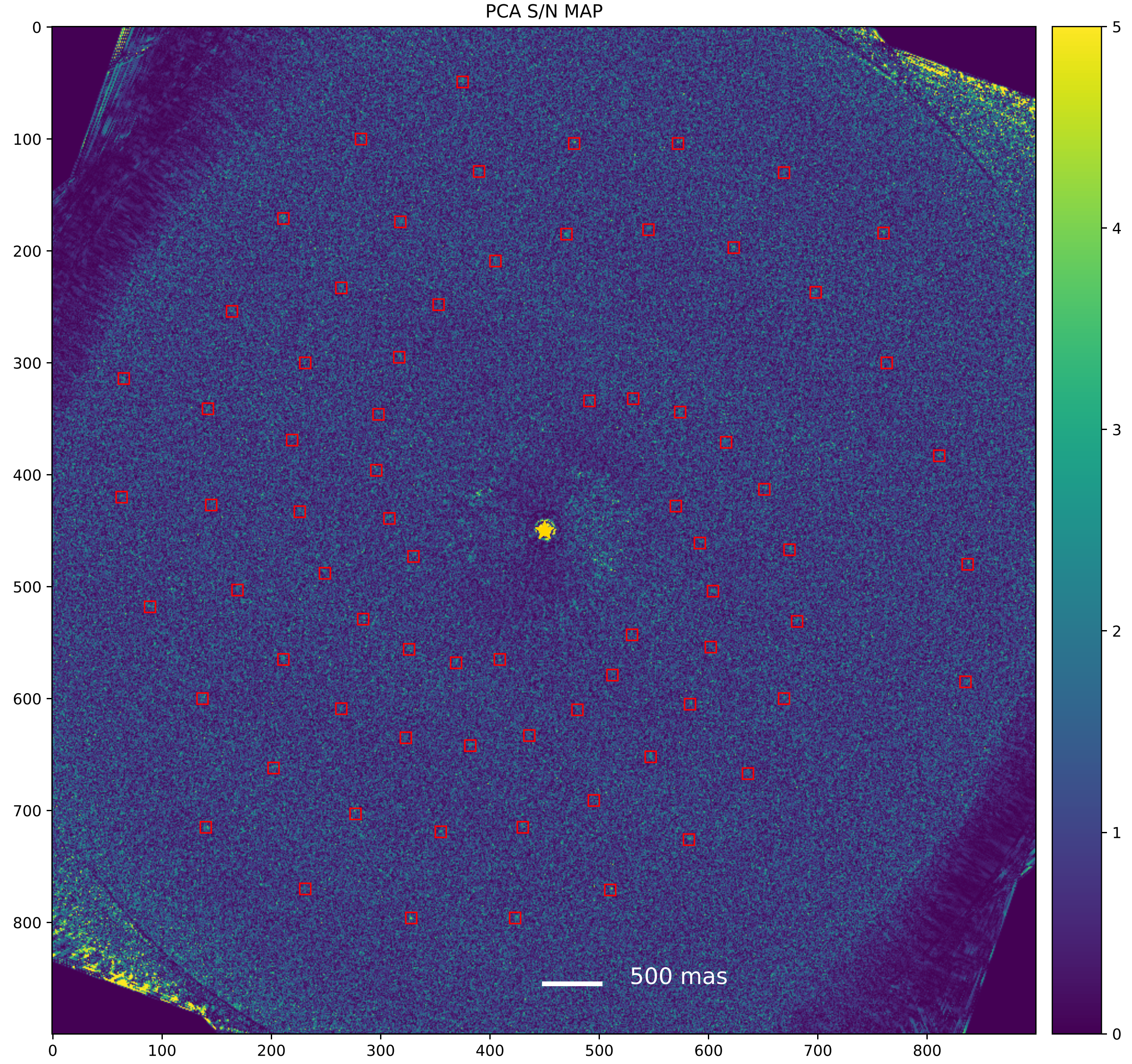

Fig. B.4: PCA S/N map. The locations of injected sources are highlighted by red boxes.

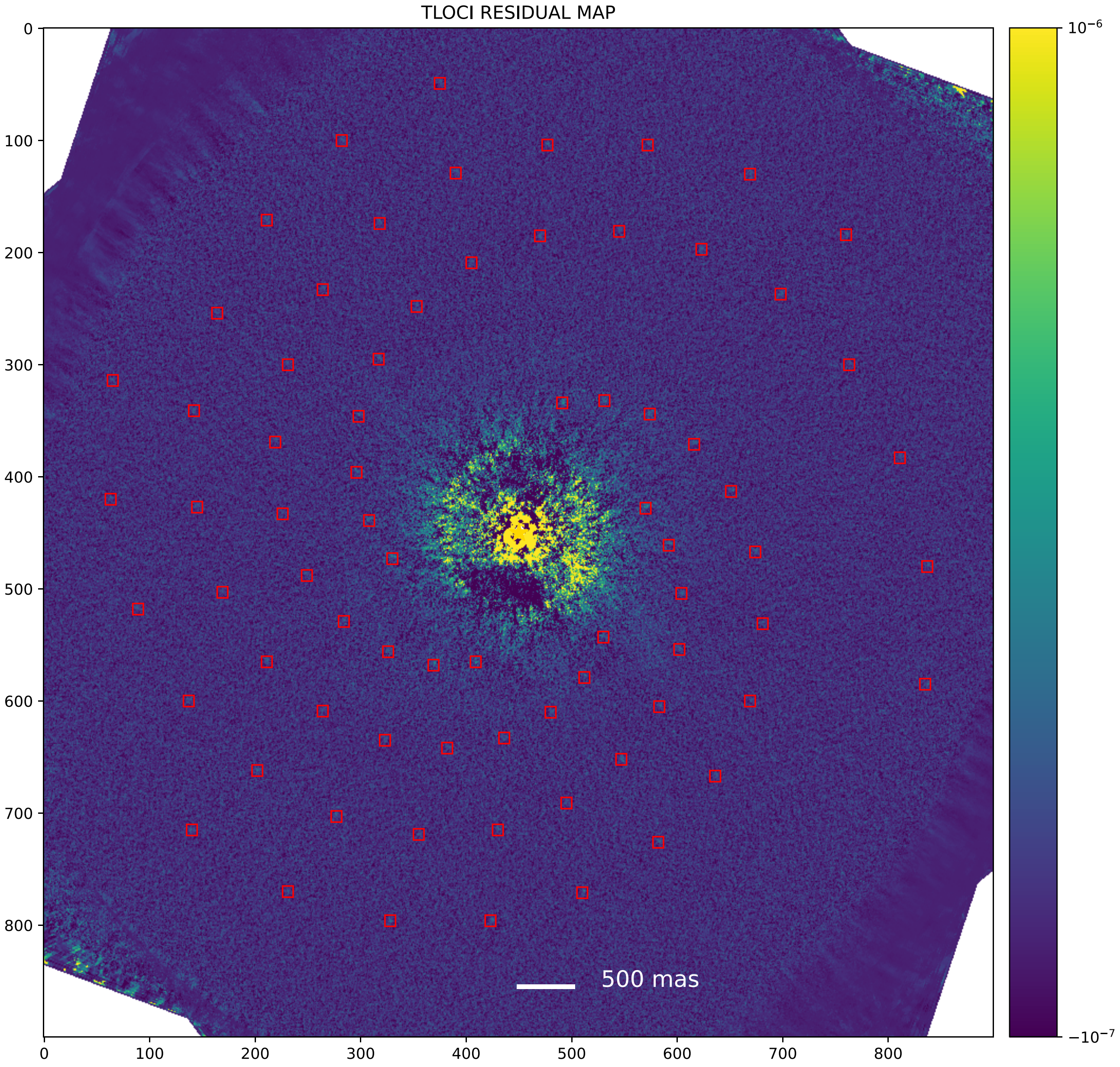

Fig. B.5: TLOCI residual map. The locations of injected sources are highlighted by red boxes.

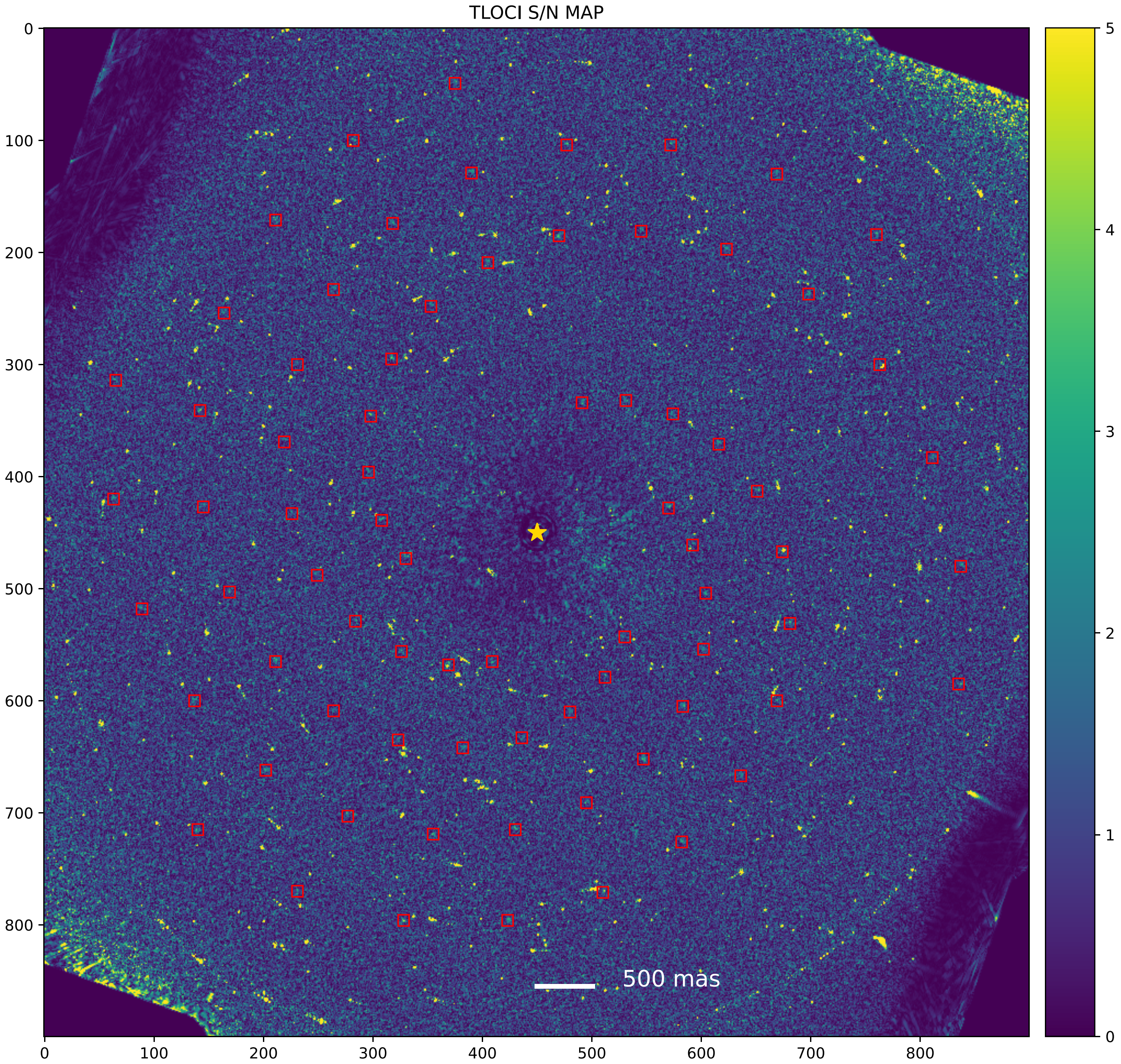

Fig. B.6: TLOCI S/N map. The locations of injected sources are highlighted by red boxes.

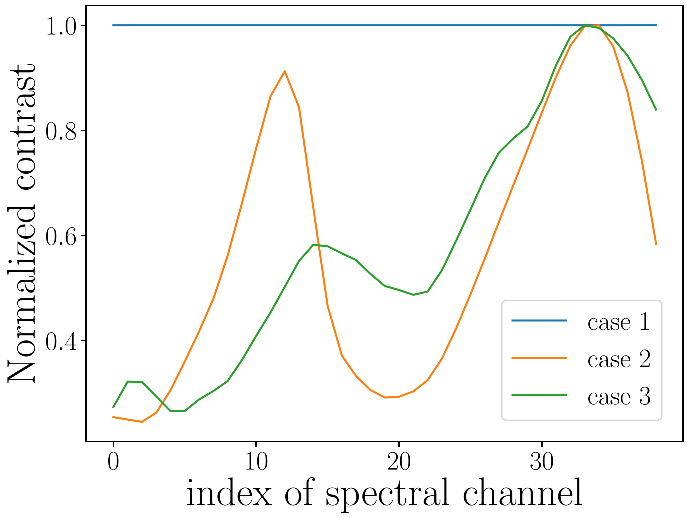

Fig. B.7: Normalized injected contrasts for IFS for the three cases considered.

CASE	SEP (mas)	PA (°)	MEAN CONTRAST	SEP (mas)	PA (°)	MEAN CONTRAST
1	200	240	6.18×10^{-6}	400	225	2.27×10^{-6}
1	600	210	1.43×10^{-6}	800	195	1.06×10^{-6}
2	200	120	3.58×10^{-6}	400	105	1.61×10^{-6}
2	600	90	1.13×10^{-6}	800	75	1.48×10^{-6}
3	200	0	2.81×10^{-6}	400	345	1.83×10^{-6}
3	600	330	1.14×10^{-6}	800	305	1.16×10^{-6}

Table B.3: IFS injected fake planets parameters.

Appendix C: MESS2 results

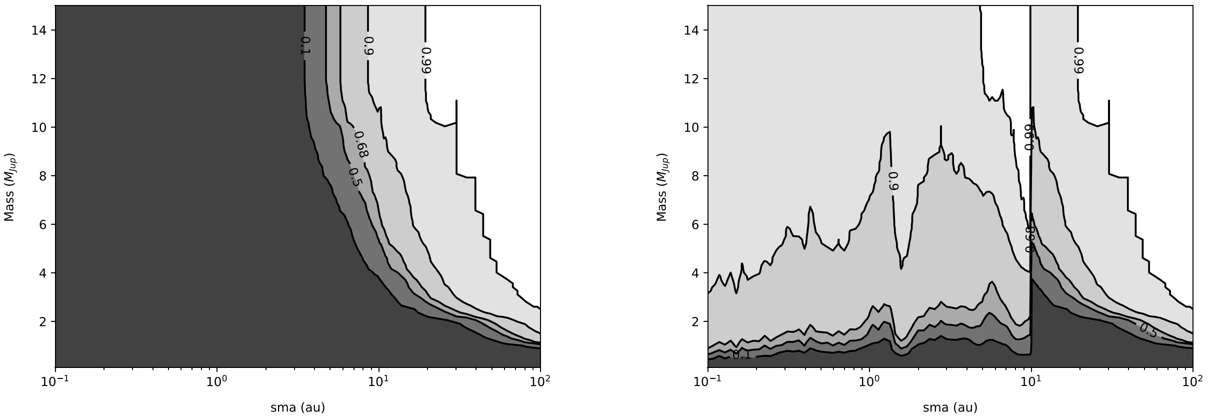

Fig. C.1: Results for HD 105, DI only (left), DI+RV (right). One epoch was available for DI.

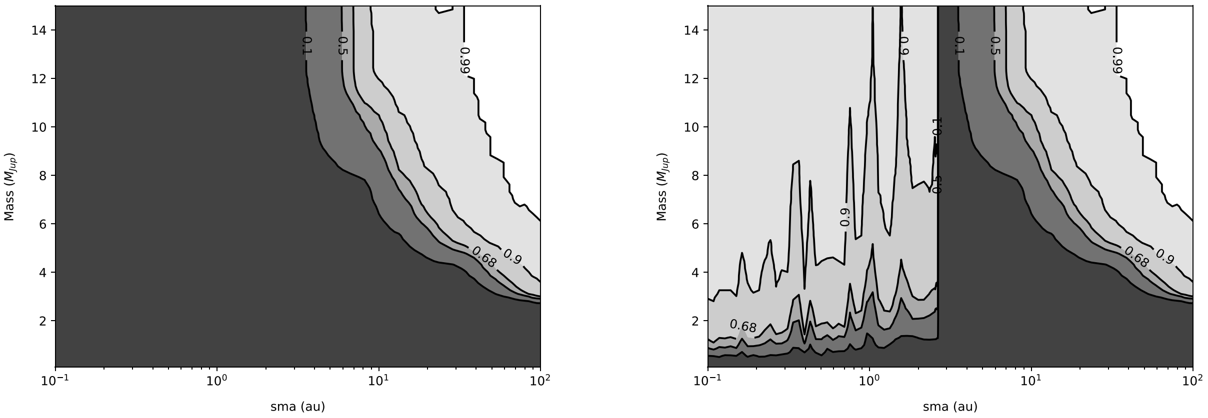

Fig. C.2: Results for HD 377, DI only (left), DI+RV (right). One epoch was available for DI.

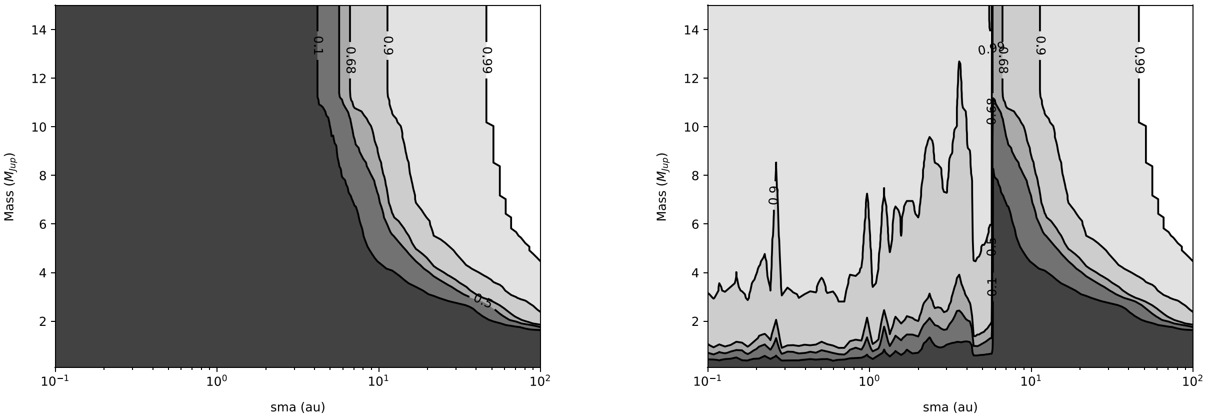

Fig. C.3: Results for HD 987, DI only (left), DI+RV (right). One epoch was available for DI.

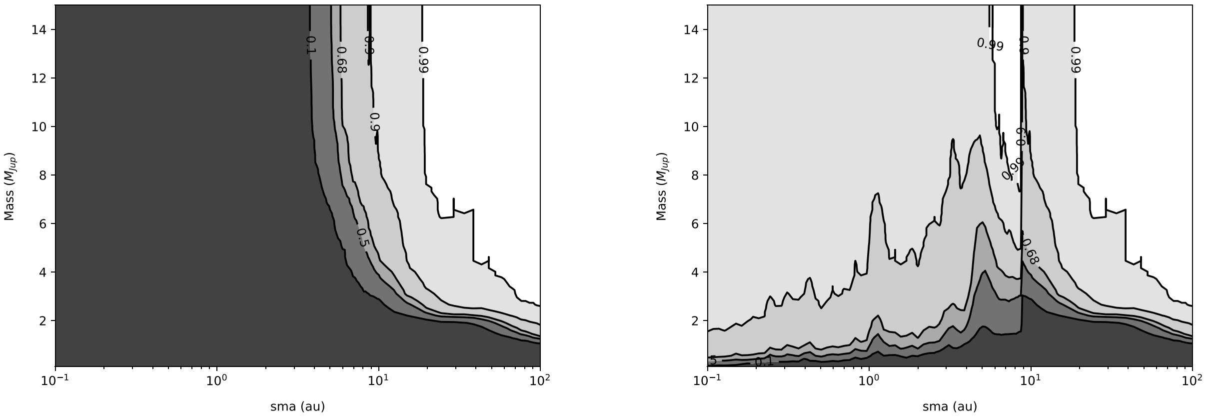

Fig. C.4: Results for HD 1466, DI only (left), DI+RV (right). Two epochs were available for DI.

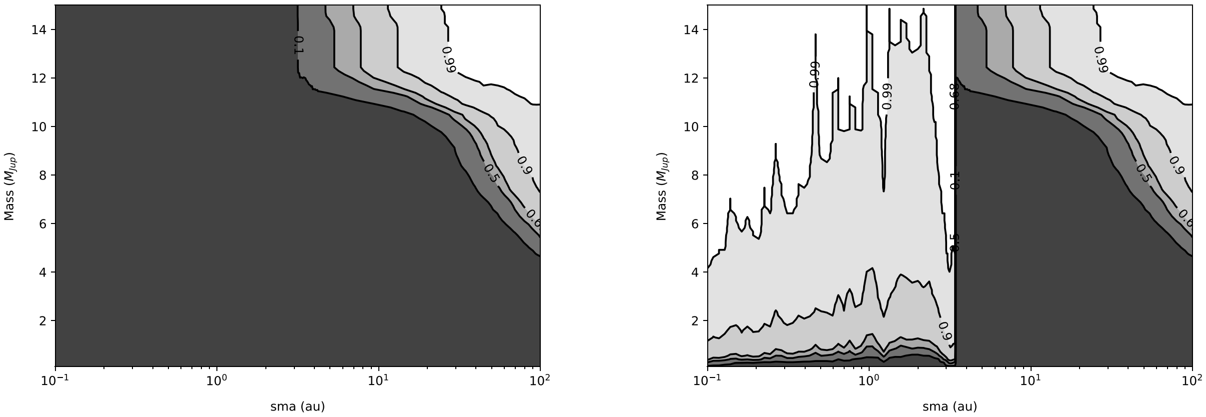

Fig. C.5: Results for BD-12 243, DI only (left), DI+RV (right). One epoch was available for DI.

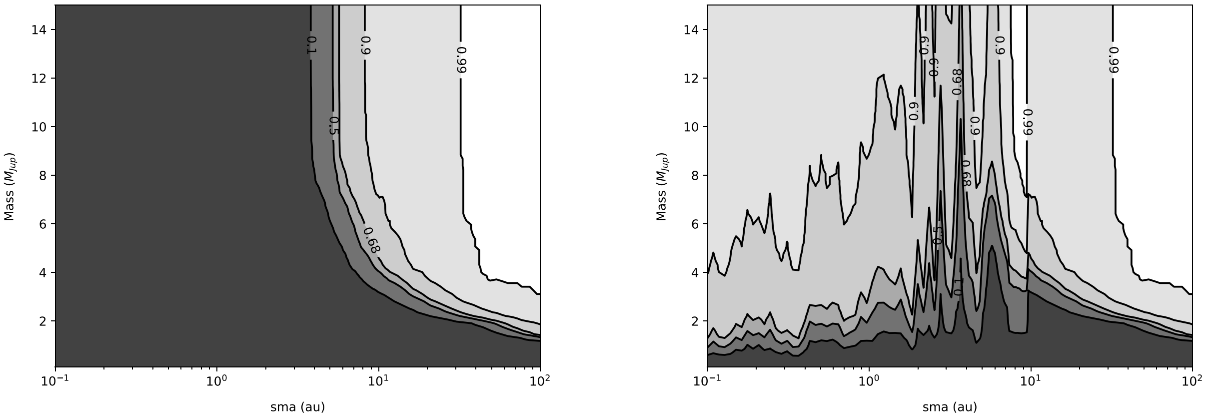

Fig. C.6: Results for HD 8558, DI only (left), DI+RV (right). Three epochs were available for DI.

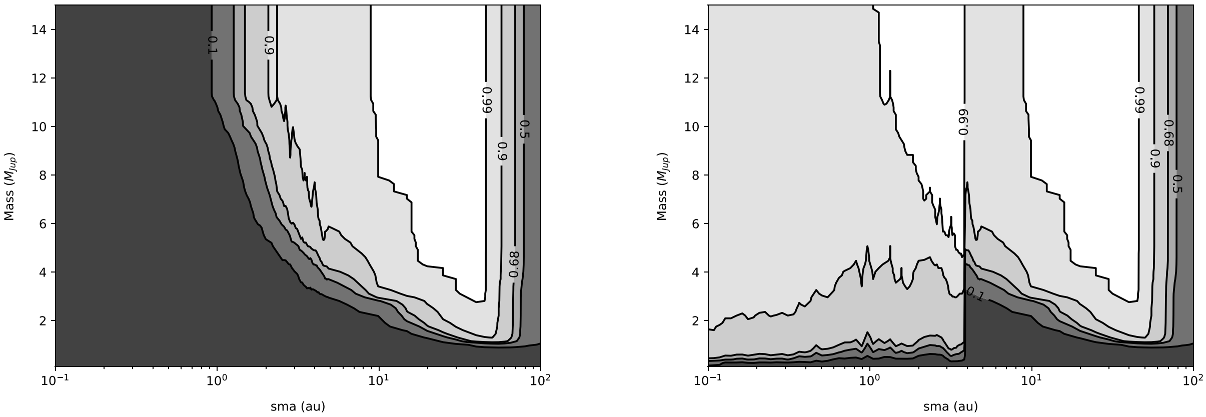

Fig. C.7: Results for HD 17925, DI only (left), DI+RV (right). One epoch was available for DI.

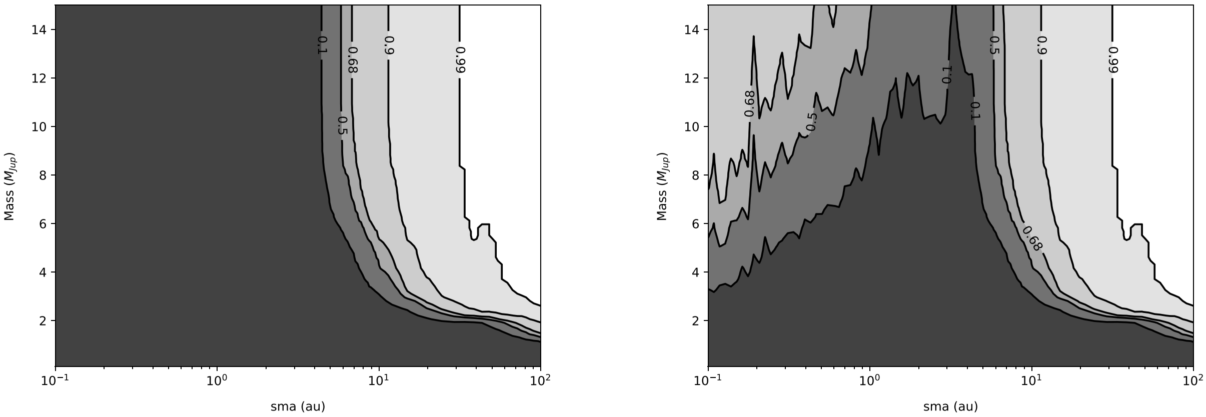

Fig. C.8: Results for HD 43989, DI only (left), DI+RV (right). Two epochs were available for DI.

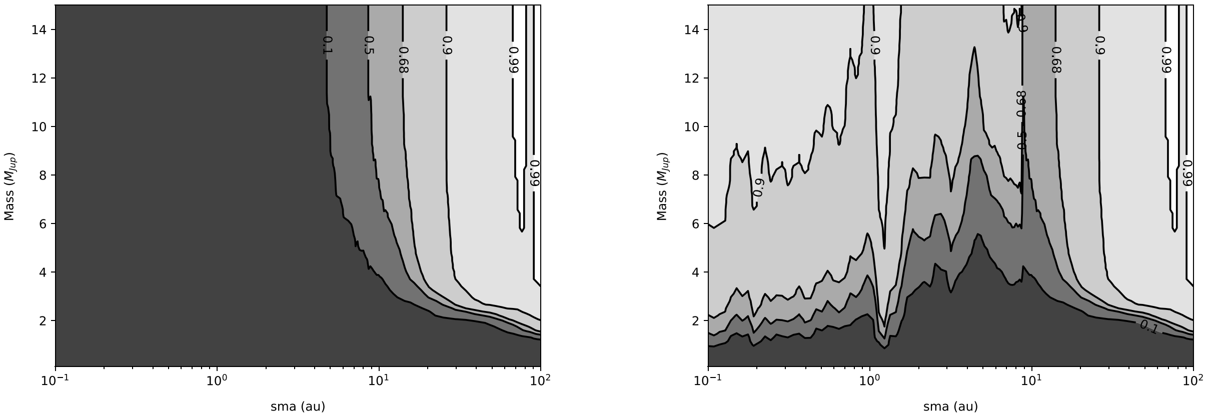

Fig. C.9: Results for HD 44627, DI only (left), DI+RV (right). One epoch was available for DI.

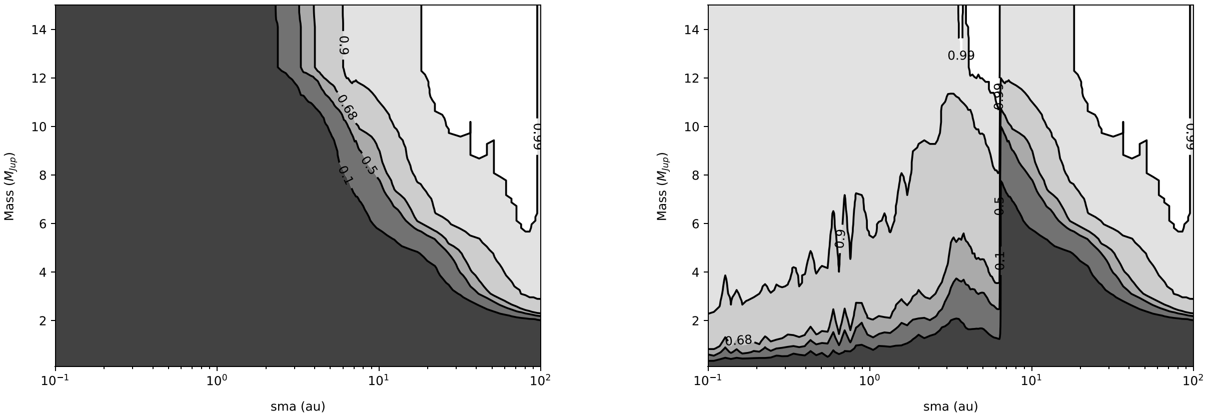

Fig. C.10: Results for HD 45270, DI only (left), DI+RV (right). One epoch was available for DI.

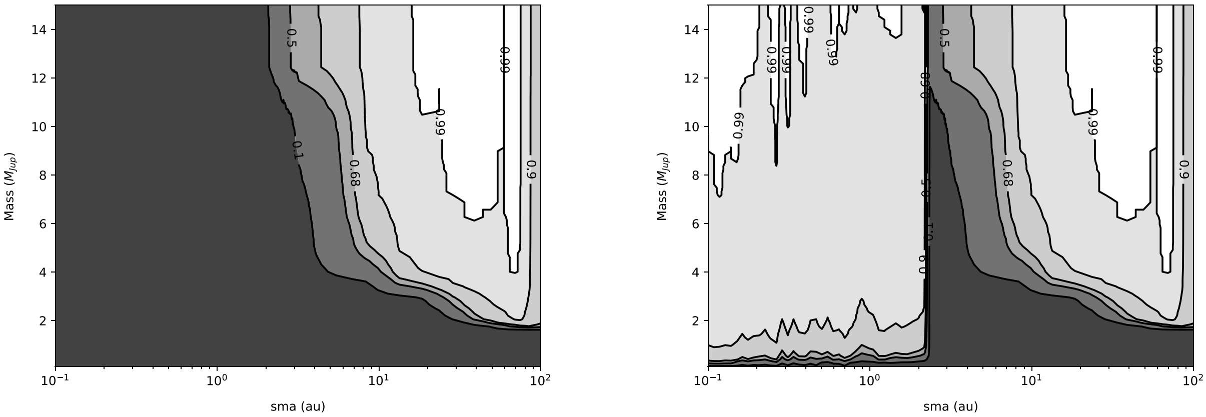

Fig. C.11: Results for CD-61 1439, DI only (left), DI+RV (right). One epoch was available for DI.

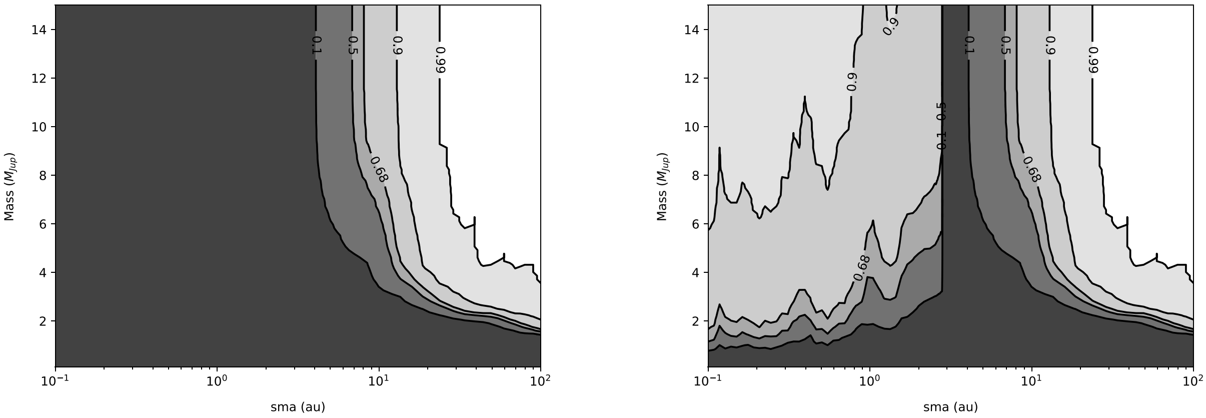

Fig. C.12: Results for HD 49855, DI only (left), DI+RV (right). One epoch was available for DI.

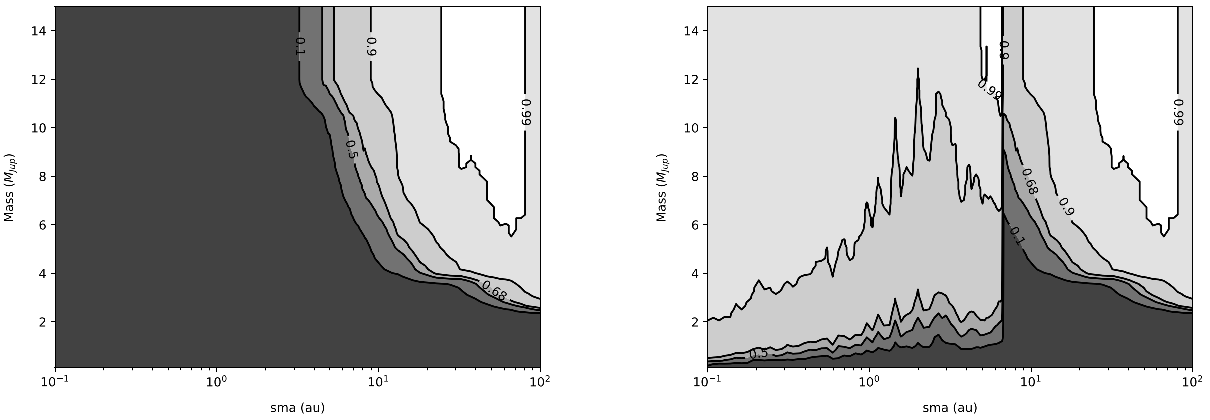

Fig. C.13: Results for HD 61005, DI only (left), DI+RV (right). One epoch was available for DI.

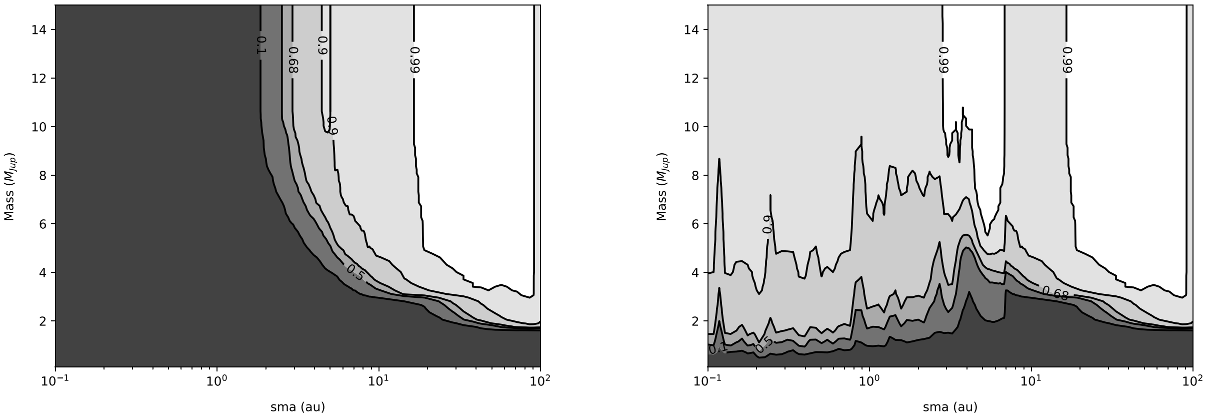

Fig. C.14: Results for HD 118100, DI only (left), DI+RV (right). One epoch was available for DI.

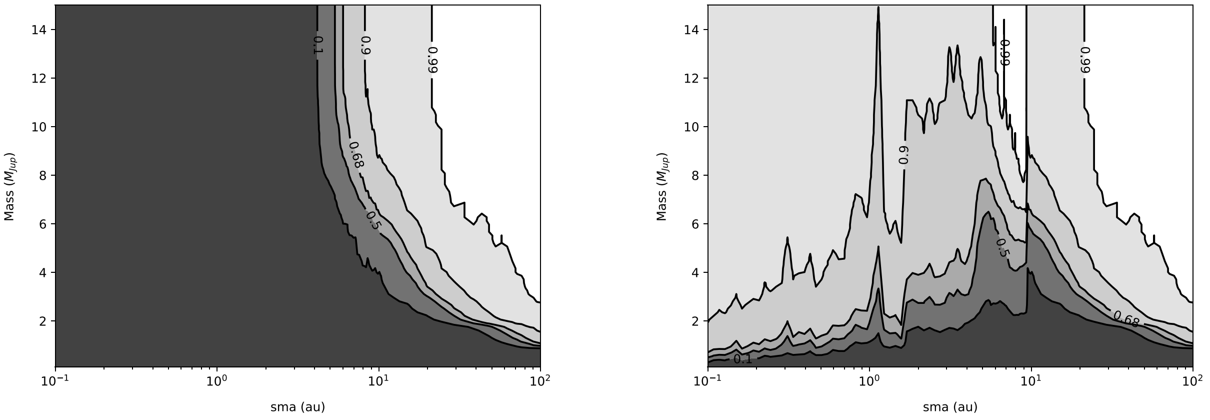

Fig. C.15: Results for HD 1642490, DI only (left), DI+RV (right). Four epochs were available for DI.

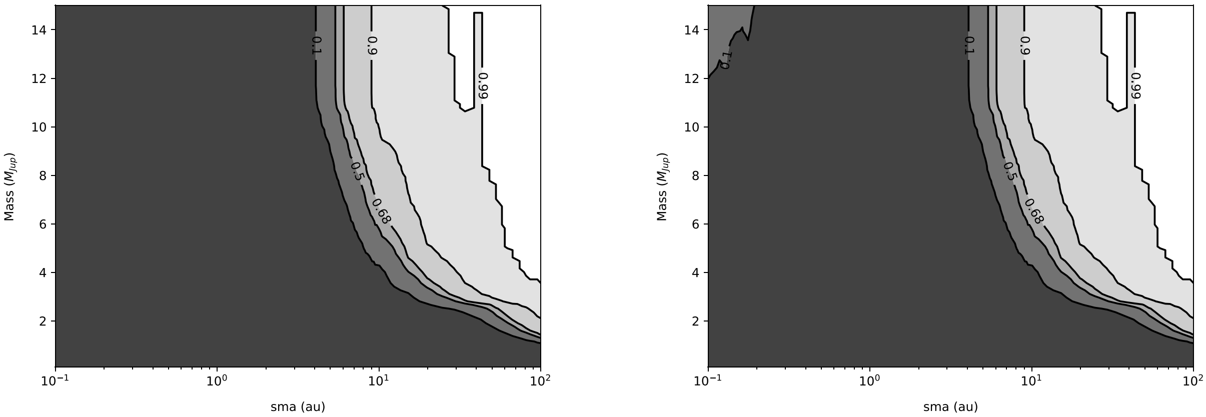

Fig. C.16: Results for HD 174429, DI only (left), DI+RV (right). Five epochs were available for DI.

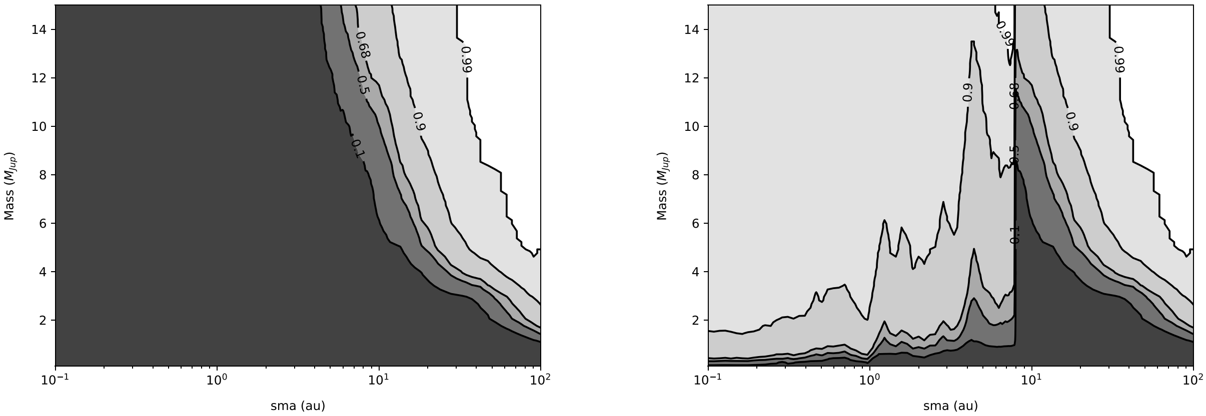

Fig. C.17: Results for HD 181327, DI only (left), DI+RV (right). One epoch was available for DI.

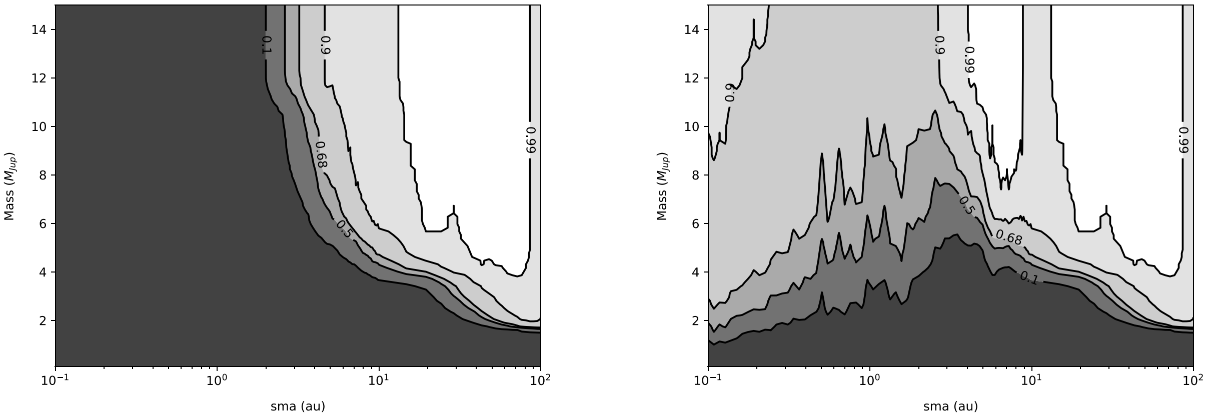

Fig. C.18: Results for HD 189245, DI only (left), DI+RV (right). One epoch was available for DI.

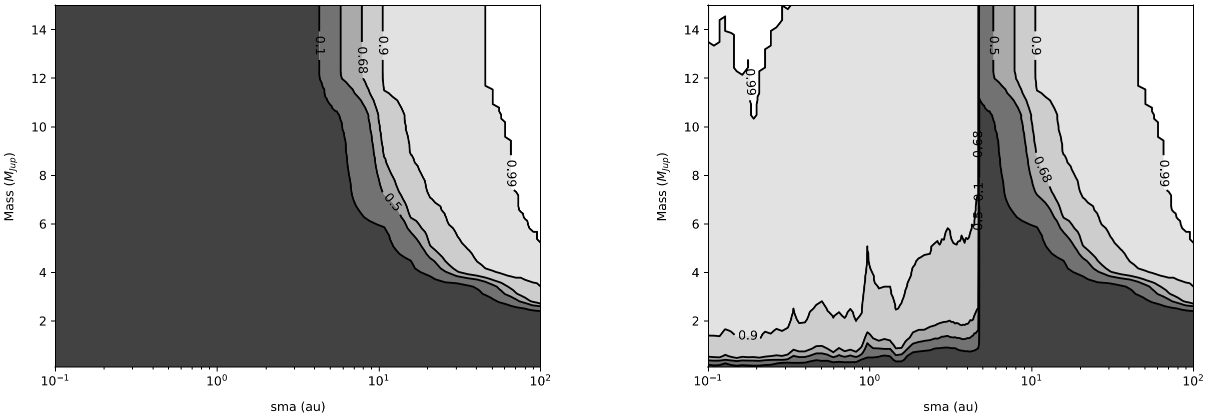

Fig. C.19: Results for HD 218860, DI only (left), DI+RV (right). One epoch was available for DI.

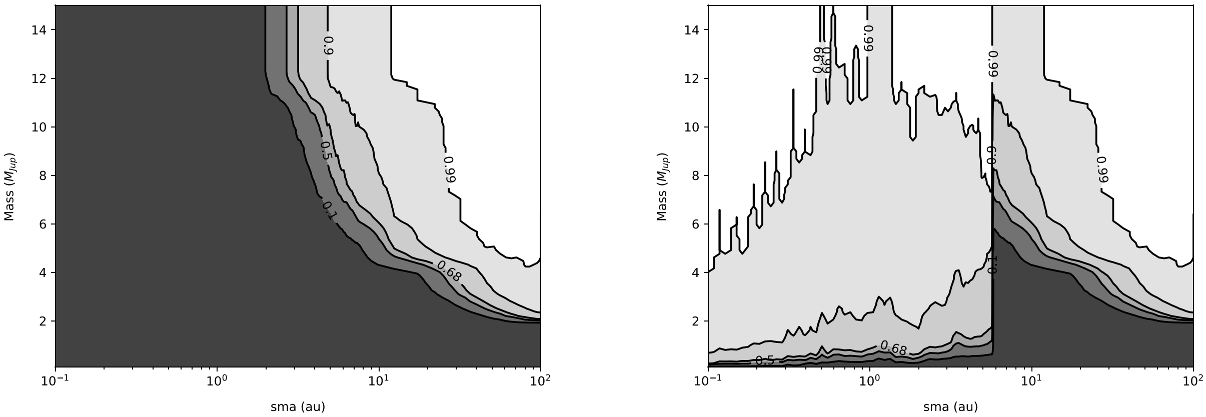

Fig. C.20: Results for HD 224228, DI only (left), DI+RV (right). One epoch was available for DI.

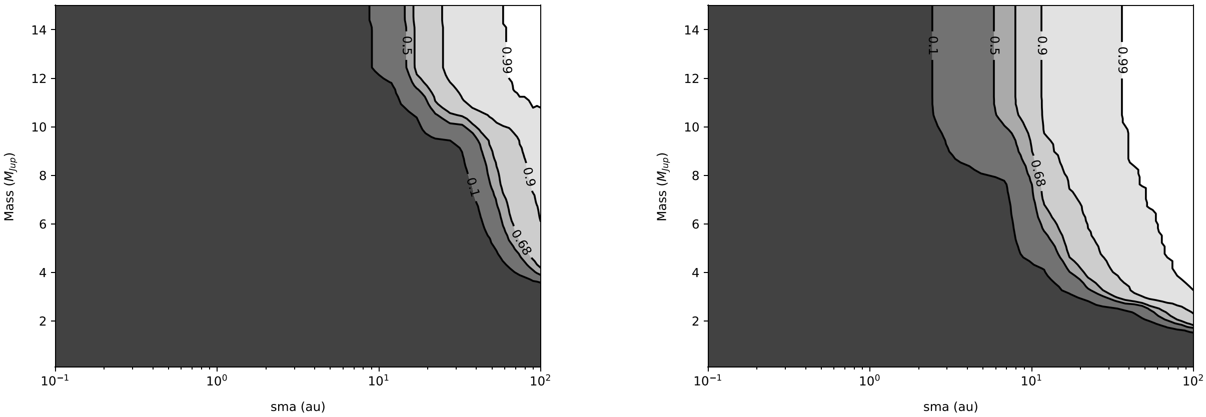

Fig. C.21: Results for HD 90712 (left) and HD 197890 (right). No radial velocity data were available. One epoch was available for DI.

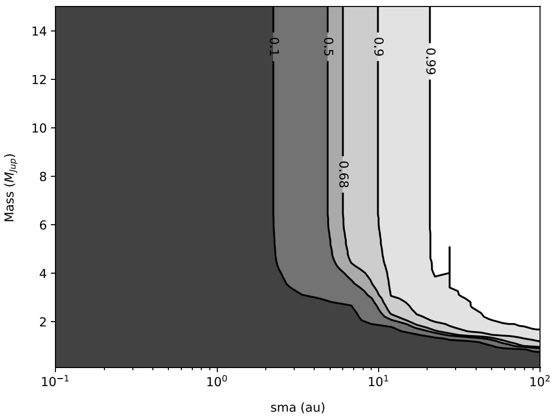

Fig. C.22: Results for CD-31 16041. No radial velocity data were available. Two epochs were available for DI.